

Cross-neutralization of SARS-CoV-2 by a human monoclonal SARS-CoV antibody

<https://doi.org/10.1038/s41586-020-2349-y>

Received: 6 April 2020

Accepted: 12 May 2020

Published online: 18 May 2020

 Check for updates

Dora Pinto^{1,9}, Young-Jun Park^{2,9}, Martina Beltramello^{1,9}, Alexandra C. Walls^{2,9}, M. Alejandra Tortorici^{2,3}, Siro Bianchi¹, Stefano Jaconi¹, Katja Culap¹, Fabrizia Zatta¹, Anna De Marco¹, Alessia Peter¹, Barbara Guarino¹, Roberto Spreafico⁴, Elisabetta Cameroni¹, James Brett Case⁵, Rita E. Chen^{5,6}, Colin Havenar-Daughton⁴, Gyorgy Snell⁴, Amalio Telenti⁴, Herbert W. Virgin⁴, Antonio Lanzavecchia^{1,7}, Michael S. Diamond^{5,6,8}, Katja Fink¹, David Veesler^{2,✉} & Davide Corti^{1,✉}

Severe acute respiratory syndrome coronavirus 2 (SARS-CoV-2) is a newly emerged coronavirus that is responsible for the current pandemic of coronavirus disease 2019 (COVID-19), which has resulted in more than 3.7 million infections and 260,000 deaths as of 6 May 2020^{1,2}. Vaccine and therapeutic discovery efforts are paramount to curb the pandemic spread of this zoonotic virus. The SARS-CoV-2 spike (S) glycoprotein promotes entry into host cells and is the main target of neutralizing antibodies. Here we describe several monoclonal antibodies that target the S glycoprotein of SARS-CoV-2, which we identified from memory B cells of an individual who was infected with severe acute respiratory syndrome coronavirus (SARS-CoV) in 2003. One antibody (named S309) potently neutralizes SARS-CoV-2 and SARS-CoV pseudoviruses as well as authentic SARS-CoV-2, by engaging the receptor-binding domain of the S glycoprotein. Using cryo-electron microscopy and binding assays, we show that S309 recognizes an epitope containing a glycan that is conserved within the *Sarbecovirus* subgenus, without competing with receptor attachment. Antibody cocktails that include S309 in combination with other antibodies that we identified further enhanced SARS-CoV-2 neutralization, and may limit the emergence of neutralization-escape mutants. These results pave the way for using S309 and antibody cocktails containing S309 for prophylaxis in individuals at a high risk of exposure or as a post-exposure therapy to limit or treat severe disease.

The entry of coronaviruses into host cells is mediated by the transmembrane S glycoprotein, which forms homotrimers that protrude from the viral surface³. The S glycoprotein comprises two functional subunits: S₁ (divided into A, B, C and D domains), which is responsible for binding to host-cell receptors; and S₂, which promotes fusion of the viral and cellular membranes^{4,5}. Both SARS-CoV-2 and SARS-CoV belong to the *Sarbecovirus* subgenus and their S glycoproteins share 80% amino acid sequence identity⁶. SARS-CoV-2 S glycoprotein is closely related to the bat SARS-related coronavirus RaTG13 S, with which it shares 97.2% amino acid sequence identity¹. It has recently been demonstrated that, in humans, angiotensin converting enzyme 2 (ACE2) is a functional receptor for SARS-CoV-2, as also is the case for SARS-CoV^{1,6–8}. Domain B of subunit S₁ (S^B) is the receptor-binding domain (RBD) of the S glycoprotein, and binds to ACE2 with high affinity, which possibly contributed to the current rapid transmission of SARS-CoV-2 in humans^{6,9} as was previously proposed for SARS-CoV¹⁰.

As the S glycoprotein of coronaviruses mediates entry into host cells, it is the main target of neutralizing antibodies and the focus of efforts

to design therapeutic agents and vaccines³. The S-glycoprotein trimers are extensively decorated with N-linked glycans that are important for protein folding¹¹ and modulate accessibility to host proteases and neutralizing antibodies^{12–17}. Previous cryo-electron microscopy (cryo-EM) structures of the SARS-CoV-2 S glycoprotein in two distinct functional states^{6,9}—along with cryo-EM and crystal structures of the SARS-CoV-2 S^B in complex with ACE2^{18–20}—have revealed dynamic states of the S^B domains, providing a blueprint for the design of vaccines and inhibitors of viral entry.

Passive administration of monoclonal antibodies (mAbs) could have a major effect on controlling the SARS-CoV-2 pandemic by providing immediate protection, complementing the development of prophylactic vaccines. Accelerated development of mAbs in a pandemic setting could be reduced to 5–6 months, compared to the traditional timeline of 10–12 months²¹. The recent finding that anuvimab (mAb114) is a safe and effective treatment for symptomatic infection with Ebola virus is a notable example of the successful use of mAb therapy during an outbreak of infectious disease^{22,23}. Potently neutralizing human mAbs

¹Humabs BioMed SA, Vir Biotechnology, Bellinzona, Switzerland. ²Department of Biochemistry, University of Washington, Seattle, WA, USA. ³Institut Pasteur and CNRS UMR 3569, Unité de Virologie Structurale, Paris, France. ⁴Vir Biotechnology, San Francisco, CA, USA. ⁵Department of Medicine, Washington University School of Medicine, St Louis, MO, USA. ⁶Department of Pathology and Immunology, Washington University School of Medicine, St Louis, MO, USA. ⁷Institute for Research in Biomedicine, Università della Svizzera Italiana, Bellinzona, Switzerland.

⁸Department of Molecular Microbiology, Washington University School of Medicine, St Louis, MO, USA. ⁹These authors contributed equally: Dora Pinto, Young-Jun Park, Martina Beltramello, Alexandra C. Walls. [✉]e-mail: dveesler@uw.edu; dcorti@vir.bio

Table 1 | Characteristics of the antibodies described in this study

mAb	VH (per cent identity)	HCDR3 sequence	VL (per cent identity)	SARS-CoV	SARS-CoV-2	Binding
S110	VH3-30 (96.88)	AKDRFQFARSWYGDYFDY	VK2-30 (96.60)	+	+	RBD and non-RBD
S124	VH2-26 (98.28)	ARINTAAAYDYDSTTFDI	VK1-39 (98.57)	+	+	RBD
S109	VH3-23 (93.75)	ARLESATQPLGYFYGMDV	VL3-25 (97.85)	+	-	RBD
S111	VH3-30 (95.14)	ARDIRHLIVVSDMDV	VK2-30 (98.30)	+	-	RBD
S127	VH3-30 (96.53)	AKDLFGYCRSTSCESLDD	VK1-9 (98.92)	+	-	RBD
S215	VH3-30 (90.28)	ARETRHYSHGLNWDFP	VK3-15 (98.92)	+	-	RBD
S217	VH3-49 (95.58)	SWIHIRVS	VK1-33 (98.21)	+	-	RBD
S218	VH3-30 (93.40)	ARDVKGHIVVMTSLDY	VK2-30 (97.62)	+	-	RBD
S219	VH1-58(92.01)	AAEMATIQNYYYYYGMDV	VK1-39 (95.34)	+	-	RBD
S222	VH1-2 (91.67)	ARGDVPVGTVWFVDF	VK1-39 (92.47)	+	-	RBD
S223	VH3-30 (95.14)	ATVSVEGYTSGWYLGTDF	VK3-15 (98.21)	+	-	RBD
S224	VH1-18 (90.97)	ARQSHSTRGGWHFSP	VK1-39 (95.70)	+	-	RBD
S225	VH3-9 (96.18)	AKDISLVFWSVNPPRNGMDV	VK1-39 (98.57)	+	-	RBD
S226	VH3-30 (89.61)	ARDSSWQSTGWPINWFDR	VK3-11 (96.11)	+	-	RBD
S227	VH3-23 (95.14)	ASPLRNYGDLLY	VK1-5 (96.06)	+	-	RBD
S228	VH3-30 (96.53)	ARDLQMRVVVSNFDY	VK2D-30 (99.32)	+	-	RBD
S230	VH3-30 (90.97)	VTQRDNRDSDYFPHFHDMDV	VK2-30 (97.62)	+	-	RBD
S231	VH3-30 (90.62)	ARDDNLDRHWPLRLGGY	VK2-30 (94.56)	+	-	RBD
S237	VH3-21 (96.53)	ARGFERYYFDS	VL1-44 (96.84)	+	-	RBD
S309	VH1-18 (97.22)	ARDYTRGAWFGESLIGGFDN	VK3-20 (97.52)	+	+	RBD
S315	VH3-7 (97.92)	ARDLWWNDQAHYYGMDV	VL3-25 (97.57)	+	+	RBD
S303	VH3-23 (90.28)	ARERDDIFPMGLNAFDI	VK1-5 (97.49)	+	+	RBD
S304	VH3-13 (97.89)	ARGDSSGYYYYFDY	VK1-39 (93.55)	+	+	RBD
S306	VH1-18 (95.49)	ASDYFDSSGYYYHSFDY	VK3-11 (98.92)	+	+	Non-RBD
S310	VH1-69 (92.71)	ATRTYDSSGYRPYYYGLDV	VL2-23 (97.57)	+	+	Non-RBD

VH and VL per cent identity refers to V gene segment identity compared to germline (as per the International Immunogenetics Information System (<http://www.imgt.org/>)).

from the memory B cells of individuals infected with SARS-CoV²⁴ or Middle East respiratory syndrome coronavirus (MERS-CoV)²⁵ have previously been isolated. Passive transfer of these mAbs protected mice challenged with various SARS-CoV isolates and SARS-related coronaviruses^{24,26,27}, as well as with MERS-CoV²⁵. Structural characterization of two of these mAbs in complex with the S-glycoprotein of SARS-CoV or MERS-CoV provided molecular-level information on the mechanisms of viral neutralization¹⁴. In particular, although both mAbs blocked S^B attachment to the host receptor, the S230 mAb (which neutralizes SARS-CoV) acted by functionally mimicking attachment to the receptor and promoting fusogenic conformational rearrangements of the S-glycoprotein¹⁴. Another mechanism of SARS-CoV neutralization has recently been described for mAb CR3022, which bound a cryptic epitope that is only accessible when at least two out of the three S^B domains of a S-glycoprotein trimer were in the open conformation^{28,29}. However, none of these mAbs neutralizes SARS-CoV-2. A mAb termed 47D11 that neutralizes SARS-CoV and SARS-CoV-2 was also recently isolated from human-immunoglobulin transgenic mice³⁰, and several mAbs have been isolated from individuals infected with SARS-CoV-2³¹.

Identifying a SARS-CoV-2 cross-neutralizing mAb

A set of human neutralizing mAbs (from an individual infected with SARS-CoV in 2003) that potently inhibit both human and zoonotic SARS-CoV isolates has previously been identified^{24,26,32}. To characterize the potential cross-reactivity of these antibodies with SARS-CoV-2, we performed a memory B cell screening using peripheral blood mononuclear cells collected in 2013 from the same patient. Here we describe 19 mAbs from the initial screen (2004 blood draw)^{24,26} and 6 mAbs from the new screen (2013 blood draw). The mAbs that we identified

had a broad usage of V gene segments, and were not clonally related (Table 1). Eight out of the twenty-five mAbs bound to CHO cells that express SARS-CoV-2 S glycoprotein or SARS-CoV S glycoprotein, with half-maximal effective concentration values that ranged between 1.4 and 6,100 ng ml⁻¹, and 0.8 and 254 ng ml⁻¹, respectively (Fig. 1a, b). We further evaluated the mAbs for binding to the SARS-CoV-2 and SARS-CoV S^B domains, as well as to the prefusion-stabilized ectodomain trimers of human coronavirus HCoV-OC43³³, MERS-CoV^{34,35}, SARS-CoV³⁵ and SARS-CoV-2⁶ S glycoproteins. None of the mAbs that we studied bound to prefusion ectodomain trimers of the HCoV-OC43 or MERS-CoV S glycoproteins, which indicated a lack of cross-reactivity outside the *Sarbecovirus* subgenus (Extended Data Fig. 1). The mAbs S303, S304, S309 and S315 bound SARS-CoV-2 and SARS-CoV RBDs with nano- to sub-picomolar affinity (Extended Data Fig. 2). In particular, the S309 IgG bound to the immobilized SARS-CoV-2 S^B domain and to the ectodomain trimer of the S-glycoprotein with sub-picomolar and picomolar avidities, respectively (Fig. 1c). The S309 Fab bound with nanomolar to sub-nanomolar affinities to both molecules (Fig. 1d). S306 and S310 stained cells that express SARS-CoV-2 S glycoprotein at higher levels than cells that express SARS-CoV S glycoprotein, yet these mAbs did not interact with ectodomain trimers and RBD constructs of SARS-CoV-2 or SARS-CoV S glycoprotein by enzyme-linked immunosorbent assay. These results suggest that S306 and S310 may recognize post-fusion SARS-CoV-2 S glycoprotein, which has recently been proposed to be abundant on the surface of authentic SARS-CoV-2 viruses³⁶ (Fig. 1a, b, Extended Data Fig. 3).

To evaluate the neutralization potency of the SARS-CoV-2 cross-reactive mAbs, we carried out pseudovirus neutralization assays using a murine leukaemia virus (MLV) pseudotyping system³⁷. S309 showed comparable neutralization potencies against both

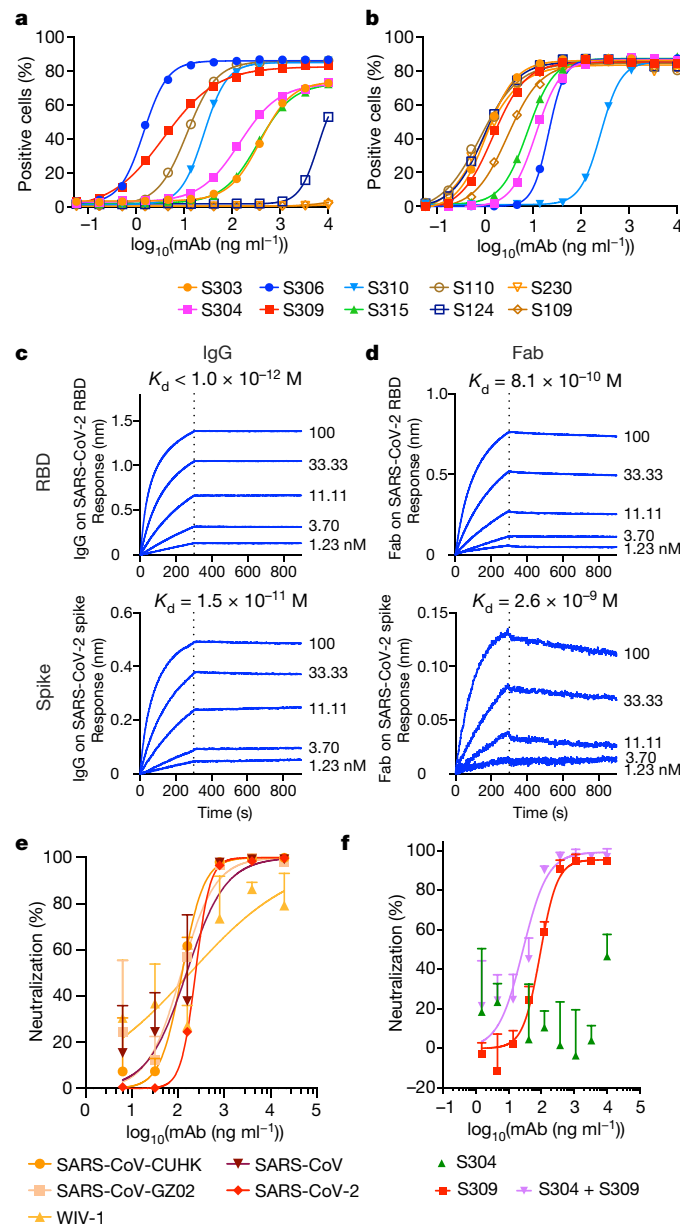


Fig. 1 | Identification of a potent SARS-CoV-2 neutralizing mAb from an individual infected with SARS-CoV. **a, b**, Binding of a panel of mAbs, isolated from a patient immune to SARS-CoV, to SARS-CoV-2 (**a**) or SARS-CoV (**b**) S glycoproteins expressed at the surface of expiCHO cells (symbols are means of duplicates from one experiment). **c, d**, Avidity and affinity measurement of S309 IgG (**c**) and Fab (**d**) for binding to immobilized SARS-CoV-2 S^B domain (RBD) and to the prefusion ectodomain trimer of S glycoprotein, measured using biolayer interferometry. **e**, Neutralization of SARS-CoV-2-MLV, SARS-CoV-MLV (bearing S glycoprotein from various isolates) and the SARS-related coronavirus WIV-1 by mAb S309. Mean \pm s.d. of triplicates is shown for all pseudoviruses, except for SARS-CoV-2 (mean of duplicates). **f**, Neutralization of authentic SARS-CoV-2 (strain n-CoV/USA_WA1/2020) by mAbs as measured by a focus-forming assay on Vero E6 cells. For the cocktail of S309 and S304, the concentration of S309 is as indicated in the x axis. S304 was added at a constant amount of 20 $\mu\text{g ml}^{-1}$. Mean \pm s.d. of quadruples is shown. In **a**, **b**, all mAbs in the same experiment were tested once. Individual mAbs were tested independently with similar results. In **c**–**f**, one representative out of two experiments with similar results is shown.

SARS-CoV and SARS-CoV-2 pseudoviruses, whereas S303 neutralized SARS-CoV-MLV but not SARS-CoV-2-MLV. S304 and S315 weakly neutralized SARS-CoV-MLV and SARS-CoV-2-MLV (Extended Data Fig. 4).

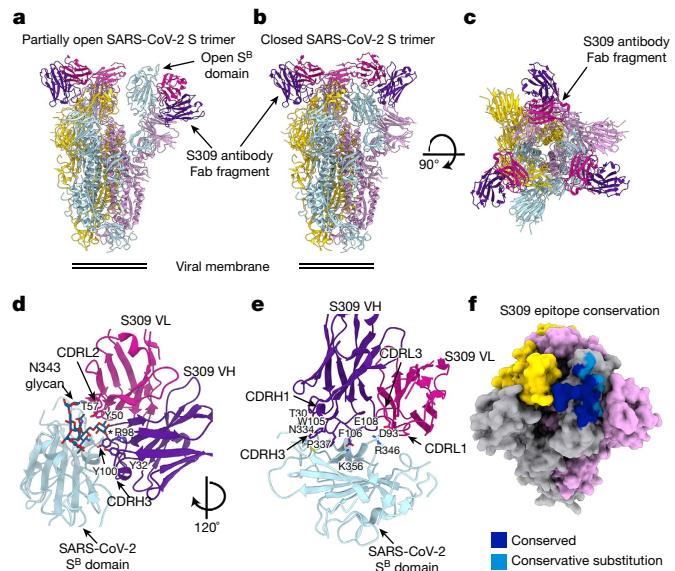


Fig. 2 | Cryo-EM structures of the SARS-CoV-2 S glycoprotein in complex with the S309 neutralizing mAb Fab fragment. **a**, Ribbon diagram of the partially open SARS-CoV-2 S-glycoprotein trimer (one S^B domain is open) bound to three S309 Fabs. The Fab bound to the open B domain is included only for visualization, and was omitted from the final model. **b**, **c**, Ribbon diagrams in two orthogonal orientations of the closed SARS-CoV-2 S-glycoprotein trimer bound to three S309 Fabs. **d**, Close-up view of the S309 epitope, showing the contacts formed with the core fucose (labelled with a star) and the rest of the glycan at position N343. **e**, Close-up view of the S309 epitope, showing the 20-residue-long CDRH3 sitting atop the S^B helix that comprises residues 337–344. The oligosaccharide at position N343 is omitted for clarity. In **a**–**e**, only the Fab variable domains are shown. In **d**, **e**, selected residues involved in interactions between S309 and SARS-CoV-2 S-glycoprotein are shown. **f**, Molecular surface representation of the SARS-CoV-2 S-glycoprotein trimer, showing the S309 epitope on one protomer coloured by residue conservation among SARS-CoV-2 and SARS-CoV S-glycoproteins. The other two protomers are coloured pink and gold.

In addition, S309 neutralized SARS-CoV-MLVs from isolates of the 3 phases of the 2002–2003 epidemic with half-maximal inhibitory concentration (IC₅₀) values of between 120 and 180 ng ml^{-1} , and partially neutralized the SARS-related coronavirus³⁸ WIV-1 (Fig. 1e). Finally, mAb S309 potently neutralized authentic SARS-CoV-2 (2019n-CoV/USA_WA1/2020) with an IC₅₀ of 79 ng ml^{-1} (Fig. 1f).

Structural basis of S309 cross-neutralization

To study the mechanisms of S309-mediated neutralization, we characterized the complex between the S309 Fab fragment and a prefusion stabilized ectodomain trimer of SARS-CoV-2 S glycoprotein⁶ using single-particle cryo-EM. Similar to a previous study of apo SARS-CoV-2 S glycoprotein⁶, 3D classification of the cryo-EM data enabled identification of two structural states: a trimer with one S^B domain open, and a closed trimer. We determined 3D reconstructions at 3.7 Å and 3.1 Å resolution, respectively, of the ectodomain trimer of the SARS-CoV-2 S glycoprotein with a single open S^B domain and in a closed state (applying three-fold symmetry), both with three S309 Fabs bound (Fig. 2a–c, Extended Data Fig. 5a–f). In parallel, we also determined a crystal structure of the S309 Fab at 3.3 Å resolution to assist model building (Extended Data Fig. 5g). The S309 Fab bound to the open S^B domain is weakly resolved in the cryo-EM map, owing to marked conformational variability of the upward pointing S^B domain, and was not modelled in density. The analysis below is based on the closed-state structure.

S309 recognizes a proteoglycan epitope on the SARS-CoV-2 S^B, distinct from the receptor-binding motif. The epitope is accessible in both

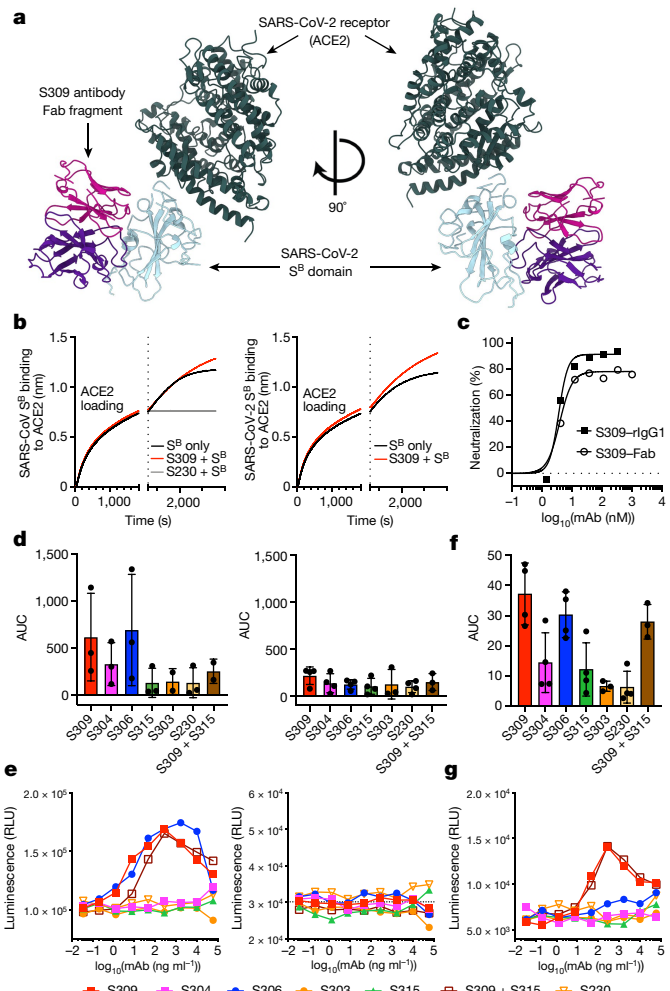


Fig. 3 | Mechanism of S309 neutralization. **a**, Ribbon diagrams of S309 and ACE2 bound to SARS-CoV-2 S^B. This composite model was generated using the SARS-CoV-2 S glycoprotein–S309 cryo-EM structure reported here, and a previously published crystal structure of SARS-CoV-2 S^B bound to ACE2²⁰. Only the Fab variable domains are shown. **b**, Competition of S309 or S230 mAbs with ACE2 to bind to SARS-CoV S^B (left) and SARS-CoV-2 S^B (right). The vertical dashed line indicates the start of the association of mAb-complexed or free S^B to solid-phase ACE2. Each mAb was tested in at least two experiments with similar results. **c**, Neutralization of SARS-CoV-MLV by S309 recombinant (r) IgG1 or S309 Fab, plotted in nM. Mean of duplicates is shown; the experiment was repeated with similar results. **d**, mAb-mediated ADCC using primary natural killer effector cells and SARS-CoV-2 S-glycoprotein-expressing expiCHO as target cells. Bars show the average area under the curve (AUC) for the responses of 3 (VV) (left) or 4 (FF-FV) (right) donors genotyped for their FcγRIII. Mean \pm s.d., data were pooled from two independent experiments. **e**, Activation of high-affinity (V158) (left) or low-affinity (F158) (right) FcγRIIIA was measured using Jurkat reporter cells and SARS-CoV-2 S-glycoprotein-expressing expiCHO as target cells. RLU, relative luminescence unit. **f**, mAb-mediated ADCP using Cell-Trace-Violet-labelled peripheral blood mononuclear cells as phagocytic cells, and PKF67-labelled SARS-CoV-2 S-glycoprotein-expressing expiCHO as target cells. Bars show the AUC for the responses of four donors. Mean \pm s.d., data were pooled from two independent experiments. **g**, Activation of FcγRIIA (131H) measured using Jurkat reporter cells and SARS-CoV-2 S-glycoprotein-expressing expiCHO as target cells. In **e** and **g**, one experiment, symbols show means of duplicates per mAb dilution except for S304, S230 and S315 (one data point per dilution). S309 was retested in an independent experiment with similar results.

the open and closed states of the S glycoprotein, which explains the stoichiometric binding of Fab to the trimer of the S glycoprotein (Fig. 2a–c). The S309 paratope is composed of all 6 complementarity-determining

region (CDR) loops, which bury a surface area of about 1,150 Å² at the interface with S^B through electrostatic interactions and hydrophobic contacts. The 20-residue-long CDR3 sits atop the S^B helix that comprises residues 337–344, and also contacts the edge of the S^B 5-stranded β-sheet (residues 356–361), overall accounting for about 50% of the buried surface area (Fig. 2d, e). CDRL1 and CDRL2 extend the epitope by interacting with the helix that spans residues 440–444, which is located near the three-fold molecular axis of the S glycoprotein. CDR3 and CDRL2 sandwich the glycan of the SARS-CoV-2 S glycoprotein at position N343, through contacts with the core fucose moiety (consistent with a previous study that detected SARS-CoV-2 N343 core-fucosylated peptides by mass spectrometry¹⁶) and to a lesser extent with the other saccharides within the glycan chain (Fig. 2d). These interactions between S309 and the glycan bury an average surface of about 300 Å² and stabilize the N343 oligosaccharide, which is resolved to a much larger extent than in structures of the apo SARS-CoV-2 S glycoprotein^{6,9}.

The structural data explain the S309 cross-reactivity between SARS-CoV-2 and SARS-CoV, as 17 out of 22 residues of the epitope are strictly conserved (Fig. 2f, Extended Data Fig. 6a, b). R346, N354, R357 and L441 of SARS-CoV-2 are conservatively substituted for K333, E341, K344 (except for SARS-CoV isolate GZ02, in which this is R444) and I428, respectively, of SARS-CoV, and the K444 of SARS-CoV-2 is semi-conservatively substituted for T431 of SARS-CoV, in agreement with the comparable binding affinities of S309 to SARS-CoV and SARS-CoV-2 S glycoprotein (Fig. 1c). The oligosaccharide at position N343 is also conserved in both viruses and corresponds to SARS-CoV N330, for which core-fucosylated glycopeptides were previously detected by mass spectrometry¹⁴ that would allow for similar interactions with the S309 Fab. Analysis of the S glycoprotein sequences of the 11,839 SARS-CoV-2 isolates reported to date indicates that the epitope residues are conserved in all but 4 isolates, for which we found N354D or the S359N substitutions that are not expected to affect recognition by S309 (Extended Data Fig. 7a, b). Furthermore, S309 contact residues are highly conserved across human and animal isolates of clade 1, 2 and 3 sarbecoviruses³⁹ (Extended Data Fig. 7c). Collectively, our data suggest that S309 could neutralize potentially all SARS-CoV-2 isolates known to be circulating to date, and possibly many other zoonotic sarbecoviruses. The degree of conservation is consistent with the moderate rates of evolution of SARS-CoV-2, estimated at about 1.8×10^{-3} substitutions per site per year⁴⁰. On the basis of more than 10^4 viral sequences analysed to date, an estimated 112 residues are under positive selection (8 in the S glycoprotein) and 18 are under negative selection (1 in the S glycoprotein) in a genome of nearly 30 kb⁴¹. These observations are consistent with the fact that *Coronaviridae* is a family of RNA viruses with unusually high replication fidelity required by their exceptionally large genomes⁴².

Mechanism of S309-mediated neutralization

The cryo-EM structure of S309 bound to SARS-CoV-2 S glycoprotein presented here, combined with the structures of SARS-CoV-2 S^B and SARS-CoV S^B in complex with ACE2, indicate^{18–20,43} that the Fab engages an epitope distinct from the receptor-binding motif and would not clash with ACE2 upon binding to S glycoprotein (Fig. 3a). Biolayer interferometry analysis of S309 Fab or IgG binding to the SARS-CoV-2 S^B domain or the ectodomain trimer of S glycoprotein confirmed the absence of competition between S309 and ACE2 for binding to the SARS-CoV-2 S glycoprotein (Fig. 3b, Extended Data Fig. 8).

To further investigate the mechanism of S309-mediated neutralization, we compared side-by-side infection of SARS-CoV-2–MLV in the presence of either S309 Fab or S309 IgG. Both experiments yielded comparable IC₅₀ values (3.8 and 3.5 nM, respectively), indicating similar potencies for IgG and Fab (Fig. 3c). However, S309 IgG-mediated neutralization reached 100%, whereas neutralization plateaued at about 80% in the presence of S309 Fab (Fig. 3c). This result indicates that one

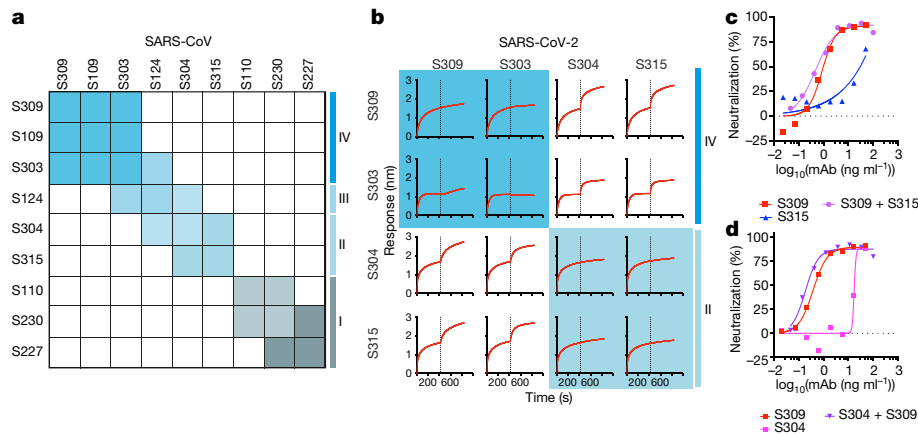


Fig. 4 | mAb cocktails enhance SARS-CoV-2 neutralization. **a**, Heat map showing the competition of mAb pairs for binding to the SARS-CoV S^B domain as measured by biolayer interferometry (as shown in Extended Data Fig. 10). **b**, Competition of mAb pairs for binding to the SARS-CoV-2 S^B domain. Each competition measured once. In **a**, **b**, a coloured box indicates competition and

each colour corresponds to an antigenic site. **c**, **d**, Neutralization of SARS-CoV-2-MLV by S309 combined with an equimolar amount of S304 or S315 mAb. For mAb cocktails, the concentration on the x axis is that of the total amount of mAb per dilution. Mean of duplicates is shown. Both experiments were repeated with similar results.

or more IgG-specific bivalent mechanisms—such as S-glycoprotein trimer cross-linking, steric hindrance or aggregation of virions⁴⁴—may contribute to the ability of S309 to fully neutralize pseudovirions.

Fc-dependent effector mechanisms, such as antibody-dependent cell cytotoxicity (ADCC) mediated by natural killer cells, can contribute to viral control in individuals infected with virus. We observed efficient S309- and S306-mediated ADCC of SARS-CoV-2 S-glycoprotein-transfected cells, whereas the other mAbs that we tested showed limited or no activity (Fig. 3d, Extended Data Fig. 9a). These findings might be related to distinct binding orientations and/or positioning of the mAb Fc fragment relative to the Fc_YRIIIa receptors. ADCC was observed only using natural killer (effector) cells that express the high-affinity Fc_YRIIIa variant (V158) but not the low-affinity variant (F158) (Fig. 3d). These results, which we confirmed using a Fc_YRIIIa cell reporter assay (Fig. 3e), suggest that S309 Fc engineering could potentially enhance the activation of natural killer cells with the low-affinity Fc_YRIIIa variant (F158)⁴⁵. Antibody-dependent cellular phagocytosis (ADCP), mediated by macrophages or dendritic cells, can contribute to viral control by clearing virus and infected cells and by stimulating a T cell response via presentation of viral antigens^{46,47}. Similar to the ADCC results, the mAbs S309 and S306 showed the strongest ADCP response (Fig. 3f, Extended Data Fig. 9b). However, Fc_YRIIIa signalling was observed only for S309 (Fig. 3g). These findings suggest that ADCP by monocytes was dependent on engagement of both Fc_YRIIIa and Fc_YRIIa. Collectively, these results demonstrate that—in addition to potent in vitro neutralization—S309 may leverage additional protective mechanisms in vivo, as has previously been shown for other antiviral antibodies^{48,49}. Although the risks of antibody-dependent disease enhancement will need to be evaluated for SARS-CoV-2, potent virus neutralization by a specific monoclonal antibody or by antibody cocktails is expected to limit this possibility, compared to weakly neutralizing antibodies that might potentially be induced upon vaccination or infection⁵⁰. Furthermore, neutralizing antibodies are associated with reduced susceptibility to re-infection or disease in humans^{51–53}. Regardless, the possibility of antibody-dependent disease enhancement will need to be assessed during clinical trials for either antibodies or vaccines.

Enhancing SARS-CoV-2 neutralization

To gain more insight into the epitopes recognized by our panel of mAbs, we used structural information, escape mutant analysis^{26,32,35} and

biolayer-interferometry-based epitope binning to map the antigenic sites that are present on the SARS-CoV and SARS-CoV-2 S^B domains (Fig. 4a, Extended Data Fig. 10). This analysis identified at least four antigenic sites within the S^B domain of SARS-CoV targeted by our panel of mAbs. The receptor-binding motif, which is targeted by S230, S227 and S110, is termed site I. Sites II and III are defined by S315 and S124, respectively, and the two sites were bridged by mAb S304. Site IV is defined by the S309, S109 and S303 mAbs. Given the lower number of mAbs that cross-react with SARS-CoV-2, we were able to identify site IV targeted by S309 and S303, and sites II and III targeted by S304 and S315 (Fig. 4b).

On the basis of these findings, we evaluated the neutralization potency of the site-IV S309 mAb in combination with either the site-II S315 mAb or the site-II and site-III S304 mAb. Although S304 and S315 alone were weakly neutralizing, the combination of either of these mAbs with S309 resulted in an enhanced neutralization potency, compared to single mAbs, against both SARS-CoV-2-MLV and authentic SARS-CoV-2 (Figs. 1f, 4c, d). A synergistic effect between two non-competing anti-RBD mAbs has previously been reported for SARS-CoV⁵⁴ and our data extend this observation to SARS-CoV-2, providing a proof-of-concept for the use of mAb combinations to prevent or control SARS-CoV-2.

In summary, our study identifies S309 as a human mAb that has broad neutralizing activity against multiple sarbecoviruses (including SARS-CoV-2), via recognition of a highly conserved epitope in the S^B domain that comprises the N343 glycan (N330 in SARS-CoV S glycoprotein). Furthermore, S309 can recruit effector mechanisms and showed increased neutralization in combination with weakly neutralizing mAbs, which may mitigate the risk of viral escape. Our data indicate the potential to discover potently neutralizing pan-sarbecovirus mAbs, define antigenic sites to include in vaccine design and pave the way to support preparedness for future outbreaks of sarbecoviruses. As S309 shows promise as an effective countermeasure to the COVID-19 pandemic caused by SARS-CoV-2, Fc variants of S309 with increased half-life and effector functions have entered an accelerated development path towards clinical trials.

Online content

Any methods, additional references, Nature Research reporting summaries, source data, extended data, supplementary information, acknowledgements, peer review information; details of author contributions

and competing interests; and statements of data and code availability are available at <https://doi.org/10.1038/s41586-020-2349-y>.

1. Zhou, P. et al. A pneumonia outbreak associated with a new coronavirus of probable bat origin. *Nature* **579**, 270–273 (2020).
2. Zhu, N. et al. A novel coronavirus from patients with pneumonia in China, 2019. *N. Engl. J. Med.* **382**, 727–733 (2020).
3. Tortorici, M. A. & Veesler, D. Structural insights into coronavirus entry. *Adv. Virus Res.* **105**, 93–116 (2019).
4. Walls, A. C. et al. Cryo-electron microscopy structure of a coronavirus spike glycoprotein trimer. *Nature* **531**, 114–117 (2016).
5. Walls, A. C. et al. Tectonic conformational changes of a coronavirus spike glycoprotein promote membrane fusion. *Proc. Natl Acad. Sci. USA* **114**, 11157–11162 (2017).
6. Walls, A. C. et al. Structure, function, and antigenicity of the SARS-CoV-2 spike glycoprotein. *Cell* **181**, 281–292.e6 (2020).
7. Hoffmann, M. et al. SARS-CoV-2 cell entry depends on ACE2 and TMPRSS2 and is blocked by a clinically proven protease inhibitor. *Cell* **181**, 271–280.e8 (2020).
8. Letko, M., Marzi, A. & Munster, V. Functional assessment of cell entry and receptor usage for SARS-CoV-2 and other lineage B betacoronaviruses. *Nat. Microbiol.* **5**, 562–569 (2020).
9. Wrapp, D. et al. Cryo-EM structure of the 2019-nCoV spike in the prefusion conformation. *Science* **367**, 1260–1263 (2020).
10. Li, W. et al. Receptor and viral determinants of SARS-coronavirus adaptation to human ACE2. *EMBO J.* **24**, 1634–1643 (2005).
11. Rossen, J. W. et al. The viral spike protein is not involved in the polarized sorting of coronaviruses in epithelial cells. *J. Virol.* **72**, 497–503 (1998).
12. Walls, A. C. et al. Glycan shield and epitope masking of a coronavirus spike protein observed by cryo-electron microscopy. *Nat. Struct. Mol. Biol.* **23**, 899–905 (2016).
13. Xiong, X. et al. Glycan shield and fusion activation of a deltacoronavirus spike glycoprotein fine-tuned for enteric infections. *J. Virol.* **92**, e01628-17 (2018).
14. Walls, A. C. et al. Unexpected receptor functional mimicry elucidates activation of coronavirus fusion. *Cell* **176**, 1026–1039 (2019).
15. Yang, Y. et al. Two mutations were critical for bat-to-human transmission of Middle East respiratory syndrome coronavirus. *J. Virol.* **89**, 9119–9123 (2015).
16. Watanabe, Y., Allen, J. D., Wrapp, D., McLellan, J. S. & Crispin, M. Site-specific analysis of the SARS-CoV-2 glycan spike. *Science* <https://doi.org/10.1126/science.abb9983> (2020).
17. Pallesen, J. et al. Immunogenicity and structures of a rationally designed prefusion MERS-CoV spike antigen. *Proc. Natl Acad. Sci. USA* **114**, E7348–E7357 (2017).
18. Yan, R. et al. Structural basis for the recognition of SARS-CoV-2 by full-length human ACE2. *Science* **367**, 1444–1448 (2020).
19. Shang, J. et al. Structural basis of receptor recognition by SARS-CoV-2. *Nature* **581**, 221–224 (2020).
20. Lan, J. et al. Structure of the SARS-CoV-2 spike receptor-binding domain bound to the ACE2 receptor. *Nature* **581**, 215–220 (2020).
21. Kelley, B. Developing therapeutic monoclonal antibodies at pandemic pace. *Nat. Biotechnol.* **38**, 540–545 (2020).
22. Corti, D. et al. Protective monotherapy against lethal Ebola virus infection by a potently neutralizing antibody. *Science* **351**, 1339–1342 (2016).
23. Levine, M. M. Monoclonal antibody therapy for Ebola virus disease. *N. Engl. J. Med.* **381**, 2365–2366 (2019).
24. Traggiai, E. et al. An efficient method to make human monoclonal antibodies from memory B cells: potent neutralization of SARS coronavirus. *Nat. Med.* **10**, 871–875 (2004).
25. Corti, D. et al. Prophylactic and postexposure efficacy of a potent human monoclonal antibody against MERS coronavirus. *Proc. Natl Acad. Sci. USA* **112**, 10473–10478 (2015).
26. Rockx, B. et al. Structural basis for potent cross-neutralizing human monoclonal antibody protection against lethal human and zoonotic severe acute respiratory syndrome coronavirus challenge. *J. Virol.* **82**, 3220–3235 (2008).
27. Menachery, V. D. et al. SARS-like WIV1-CoV poised for human emergence. *Proc. Natl Acad. Sci. USA* **113**, 3048–3053 (2016).
28. Yuan, M. et al. A highly conserved cryptic epitope in the receptor binding domains of SARS-CoV-2 and SARS-CoV. *Science* **368**, 630–633 (2020).
29. Joyce, M. G. et al. A cryptic site of vulnerability on the receptor binding domain of the SARS-CoV-2 spike glycoprotein. Preprint at bioRxiv <https://doi.org/10.1101/2020.03.15.992883> (2020).
30. Wang, C. et al. A human monoclonal antibody blocking SARS-CoV-2 infection. *Nat. Commun.* **11**, 2251 (2020).
31. Ju, B., Zhang, Q., Ge, J. et al. Human neutralizing antibodies elicited by SARS-CoV-2 infection. *Nature* <https://doi.org/10.1038/s41586-020-2380-z> (2020).
32. Rockx, B. et al. Escape from human monoclonal antibody neutralization affects in vitro and in vivo fitness of severe acute respiratory syndrome coronavirus. *J. Infect. Dis.* **201**, 946–955 (2019).
33. Tortorici, M. A. et al. Structural basis for human coronavirus attachment to sialic acid receptors. *Nat. Struct. Mol. Biol.* **26**, 481–489 (2019).
34. Park, Y. J. et al. Structures of MERS-CoV spike glycoprotein in complex with sialoside attachment receptors. *Nat. Struct. Mol. Biol.* **26**, 1151–1157 (2019).
35. Walls, A. C. et al. Unexpected receptor functional mimicry elucidates activation of coronavirus fusion. *Cell* **176**, 1026–1039.e15 (2019).
36. Liu, C. et al. Viral architecture of SARS-CoV-2 with post-fusion spike revealed by cryo-EM. Preprint bioRxiv <https://doi.org/10.1101/2020.03.02.972927> (2020).
37. Millet, J. K. & Whittaker, G. R. Murine leukemia virus (MLV)-based coronavirus spike-pseudotyped particle production and infection. *Bio. Protoc.* **6**, e2035 (2016).
38. Ge, X. Y. et al. Isolation and characterization of a bat SARS-like coronavirus that uses the ACE2 receptor. *Nature* **503**, 535–538 (2013).
39. Lu, R. et al. Genomic characterisation and epidemiology of 2019 novel coronavirus: implications for virus origins and receptor binding. *Lancet* **395**, 565–574 (2020).
40. Li, X. et al. Transmission dynamics and evolutionary history of 2019-nCoV. *J. Med. Virol.* **92**, 501–511 (2020).
41. Pond, S. SARS-CoV-2 Natural Selection Analysis. <http://data.hyphy.org/web/covid-19/dashboard/> (2020).
42. Smith, E. C., Sexton, N. R. & Denison, M. R. Thinking outside the triangle: replication fidelity of the largest RNA viruses. *Annu. Rev. Virol.* **1**, 111–132 (2014).
43. Li, F., Li, W., Farzan, M. & Harrison, S. C. Structure of SARS coronavirus spike receptor-binding domain complexed with receptor. *Science* **309**, 1864–1868 (2005).
44. Klasse, P. J. & Sattentau, Q. J. Occupancy and mechanism in antibody-mediated neutralization of animal viruses. *J. Gen. Virol.* **83**, 2091–2108 (2002).
45. Wang, X., Mathieu, M. & Brezski, R. J. IgG Fc engineering to modulate antibody effector functions. *Protein Cell* **9**, 63–73 (2018).
46. He, W. et al. Alveolar macrophages are critical for broadly-reactive antibody-mediated protection against influenza A virus in mice. *Nat. Commun.* **8**, 846 (2017).
47. DiLillo, D. J. & Ravetch, J. V. Differential Fc-receptor engagement drives an anti-tumor vaccine effect. *Cell* **161**, 1035–1045 (2015).
48. Corti, D. et al. A neutralizing antibody selected from plasma cells that binds to group 1 and group 2 influenza A hemagglutinins. *Science* **333**, 850–856 (2011).
49. Hessel, A. J. et al. Fc receptor but not complement binding is important in antibody protection against HIV. *Nature* **449**, 101–104 (2007).
50. Iwasaki, A. & Yang, Y. The potential danger of suboptimal antibody responses in COVID-19. *Nat. Rev. Immunol.* **20**, 339–341 (2020).
51. Callow, K. A. Effect of specific humoral immunity and some non-specific factors on resistance of volunteers to respiratory coronavirus infection. *J. Hyg. (Lond.)* **95**, 173–189 (1985).
52. Reed, S. E. The behaviour of recent isolates of human respiratory coronavirus in vitro and in volunteers: evidence of heterogeneity among 229E-related strains. *J. Med. Virol.* **13**, 179–192 (1984).
53. Callow, K. A., Parry, H. F., Sergeant, M. & Tyrrell, D. A. The time course of the immune response to experimental coronavirus infection of man. *Epidemiol. Infect.* **105**, 435–446 (1990).
54. ter Meulen, J. et al. Human monoclonal antibody combination against SARS coronavirus: synergy and coverage of escape mutants. *PLoS Med.* **3**, e237 (2006).

Publisher's note Springer Nature remains neutral with regard to jurisdictional claims in published maps and institutional affiliations.

© The Author(s), under exclusive licence to Springer Nature Limited 2020

Article

Methods

No statistical methods were used to predetermine sample size. The experiments were not randomized and investigators were not blinded to allocation during experiments and outcome assessment.

Cell lines

Cell lines used in this study were obtained from ATCC (HEK293T, Vero-E6, Vero CCL81 cells) or Invitrogen (Expi-CHO cells). All cell lines used in this study were routinely tested for mycoplasma and found to be mycoplasma-free.

Ethics statement

Donors provided written informed consent for the use of blood and blood components (such as sera), following approval by the Canton Ticino Ethics Committee (Switzerland).

Antibody discovery and expression

mAbs were isolated from Epstein–Barr-virus-immortalized memory B cells. Recombinant antibodies were expressed in ExpiCHO cells transiently cotransfected with plasmids expressing the heavy and light chain, as previously described⁵⁵. The mAbs S303, S304, S306, S309, S310 and S315 were expressed as recombinant IgG-LS antibodies. The LS mutation confers a longer half-life in vivo⁵⁶. Antibodies S110 and S124 tested in Fig. 1 and Extended Data Fig. 1 were purified mAbs produced from immortalized B cells.

Transient expression of recombinant SARS-CoV-2 protein and flow cytometry

The full-length S gene of SARS-CoV-2 strain (SARS-CoV-2-S) isolate BetaCoV/Wuhan-Hu-1/2019 (accession number MN908947) was codon-optimized for human cell expression and cloned into the phCMV1 expression vector (Genlantis). Expi-CHO cells were transiently transfected with phCMV1-SARS-CoV-2-S, SARS-spike_pcDNA-3.1 (strain SARS) or empty phCMV1 (mock) using ExpiFectamine CHO Enhancer. Two days after transfection, cells were collected for immunostaining with mAbs. An Alexa-647-labelled secondary antibody anti-human IgG Fc was used for detection. Binding of mAbs to transfected cells was analysed by flow cytometry using a ZE5 Cell Analyzer (Biorad) and FlowJo software (TreeStar). Positive binding was defined by differential staining of CoV-S-glycoprotein transfectants versus mock transfectants.

Affinity and avidity determination and competition experiments using Octet (biolayer interferometry)

For affinity and avidity determination of IgG1 compared to Fab fragment, biotinylated RBD of SARS-CoV-2 (produced in house; residues 331–550 of S glycoprotein from BetaCoV/Wuhan-Hu-1/2019, accession number MN908947, biotinylated with EZ-Link NHS-PEG₄-biotin from ThermoFisher) and biotinylated SARS-CoV-2 2PS glycoprotein avi-tagged were loaded at 7.5 µg/ml in kinetics buffer (0.01% endotoxin-free BSA, 0.002% Tween-20, 0.005% NaN₃ in PBS) for 8 min onto streptavidin biosensors (Molecular Devices, ForteBio). Association of IgG1 and Fab was performed in kinetics buffer at 100, 33, 11, 3.6, 1.2 nM for 5 min. Dissociation in kinetics buffer was measured for 10 min. K_d values were calculated using a 1:1 global fit model (Octet).

Alternatively, measurement of apparent K_d for IgGs was determined using protein A biosensors (Pall ForteBio) that were loaded with different mAbs at 2.7 µg/ml for 1 min, after a hydration step for 10 min in kinetics buffer. Association curves were recorded for 5 min by incubating the mAb-coated sensors with different concentrations of SARS-CoV RBD (Sino Biological) or SARS-CoV-2 RBD (produced in house; residues 331–550 of S glycoprotein from BetaCoV/Wuhan-Hu-1/2019, accession number MN908947). The highest RBD concentration was 10 µg/ml, then serially diluted 1:2.5. Dissociation was recorded for 9 min by moving the sensors to wells containing kinetics buffer. K_d values were

calculated using a global fit model (Octet). Octet Red96 (ForteBio) equipment was used.

For mAb competition experiments, His-tagged RBD of SARS-CoV or SARS-CoV-2 was loaded for 5 min at 3 µg/ml in kinetics buffer onto anti-Penta-HIS (HIS1K) biosensors (Molecular Devices, ForteBio). Association of mAbs was performed in kinetics buffer at 15 µg/ml.

For ACE2 competition experiments, ACE2-His (Bio-Techne AG) was loaded for 30 min at 5 µg/ml in kinetics buffer onto anti-HIS (HIS2) biosensors (Molecular Devices-ForteBio).

SARS-CoV RBD–rabbit Fc or SARS-CoV-2 RBD–mouse Fc (Sino Biological Europe GmbH) at 1 µg/ml was associated for 15 min, after pre-incubation with or without antibody (30 µg/ml, 30 min). Dissociation was monitored for 5 min.

Enzyme-linked immunosorbent assay

The following proteins were coated on 96-well enzyme-linked immunosorbent assay plates at the following concentrations: SARS-CoV RBD (Sino Biological, 40150-V08B1) at 1 µg/ml, SARS-CoV-2 RBD (produced in house) at 10 µg/ml, ectodomains (stabilized prefusion trimer) of SARS-CoV, SARS-CoV-2, HCoV-OC43 and MERS-CoV, all at 1 µg/ml. After blocking with 1% BSA in PBS, antibodies were added to the plates at concentrations between 5 and 0.000028 µg/ml and incubated for 1 h at room temperature. Plates were washed and secondary antibody Goat Anti Human IgG-AP (Southern Biotechnology: 2040-04) was added. Substrate p-nitrophenyl pPhosphate (pNPP) (Sigma-Aldrich 71768) was used for colour development. Optical density at 405 nm was read on an ELx808IU plate reader (Biotek).

Measurement of Fc-mediated effector functions

ADCC assays were performed using ExpiCHO cells transiently transfected with SARS-CoV or SARS-CoV-2 S glycoprotein as targets. Natural killer cells were isolated from fresh blood of healthy donors using the MACSxpress NK Isolation Kit (Miltenyi Biotec, cat. no. 130-098-185). Target cells were incubated with titrated concentrations of mAbs for 10 min and were then incubated with primary human natural killer cells as effector cells at an effector:target ratio of 9:1. ADCC was measured using LDH release assay (Cytotoxicity Detection Kit (LDH) (Roche; cat. no. 11644793001)) after 4 h incubation at 37 °C.

ADCP assays were performed using ExpiCHO target cells transiently transfected with SARS-CoV-2 S glycoprotein and fluorescently labelled with PKH67 Fluorescent Cell Linker Kits (Sigma Aldrich, cat. no. MINI67). Target cells were incubated with titrated concentrations of mAbs for 10 min, followed by incubation with human peripheral blood mononuclear cells isolated from healthy donors and fluorescently labelled with Cell Trace Violet (Invitrogen, cat. no. C34557). An effector:target ratio of 20:1 was used. After an overnight incubation at 37 °C, cells were stained with anti-human CD14-APC antibody (BD Pharmingen, cat. no. 561708, Clone M5E2) to stain monocytes. Antibody-mediated phagocytosis was determined by flow cytometry, gating on CD14⁺ cells that were double-positive for cell trace violet and PKH67.

Determination of mAb-dependent activation of human Fc_YRIIIa or Fc_YRIIa was performed using ExpiCHO cells transiently transfected with SARS-CoV-2 S glycoprotein (BetaCoV/Wuhan-Hu-1/2019). Cells were incubated with titrated concentrations of mAbs for 10 min before incubation with Fc_YRIIIa-receptor- or Fc_YRIIa-expressing Jurkat cells stably transfected with NFAT-driven luciferase gene (Promega, cat. no. G9798 and G7018). An effector-to-target ratio of 6:1 for Fc_YRIIIa and 5:1 for Fc_YRIIa was used. Activation of human Fc_YR in this bioassay results in the NFAT-mediated expression of a luciferase reporter gene. Luminescence was measured after 21 h of incubation at 37 °C with 5% CO₂ using the Bio-Glo-TM Luciferase Assay Reagent according to the manufacturer's instructions.

Pseudovirus neutralization assays

MLV-based SARS-CoV S-glycoprotein-pseudotyped viruses were prepared as previously described^{6,37}. HEK293T cells were

cotransfected with a SARS-CoV, SARS-CoV-2, CUHK, GZ02 or WiV1 S-glycoprotein-encoding plasmid, an MLV Gag-Pol packaging construct and the MLV transfer vector encoding a luciferase reporter using the Lipofectamine 2000 transfection reagent (Life Technologies) according to the manufacturer's instructions. Cells were incubated for 5 h at 37 °C with 8% CO₂ with OPTIMEM transfection medium. DMEM containing 10% FBS was added for 72 h.

VeroE6 cells or DBT cells transfected with human ACE2 were cultured in DMEM containing 10% FBS, 1% penicillin–streptomycin and plated into 96-well plates for 16–24 h. Concentrated pseudovirus with or without serial dilution of antibodies was incubated for 1 h and then added to the wells after washing 3× with DMEM. After 2–3 h DMEM containing 20% FBS and 2% penicillin–streptomycin was added to the cells for 48 h. Following 48 h of infection, One-Glo-EX (Promega) was added to the cells and incubated in the dark for 5–10 min before reading on a Varioskan LUX plate reader (ThermoFisher). Measurements were done in duplicate and relative luciferase units were converted to per cent neutralization and plotted with a nonlinear regression curve fit in PRISM.

Live virus neutralization assay

SARS-CoV-2 strain 2019-nCoV/USA_WA1/2020 was obtained from the Centers for Disease Control and Prevention (gift of N. Thornburg). Virus was passaged once in Vero CCL81 cells (ATCC) and titrated by focus-forming assay on Vero E6 cells. Serial dilutions of the indicated mAbs were incubated with 10² focus-forming units of SARS-CoV-2 for 1 h at 37 °C. Mab–virus complexes were added to Vero E6 cell monolayers in 96-well plates and incubated at 37 °C for 1 h. Subsequently, cells were overlaid with 1% (w/v) methylcellulose in MEM supplemented with 2% FBS. Plates were collected 30 h later by removing overlays and fixed with 4% PFA in PBS for 20 min at room temperature. Plates were washed and sequentially incubated with 1 µg/ml of CR3022⁵⁷ anti-S-glycoprotein antibody and HRP-conjugated goat anti-human IgG in PBS supplemented with 0.1% saponin and 0.1% BSA. SARS-CoV-2-infected cell foci were visualized using TrueBlue peroxidase substrate (KPL) and quantified on an ImmunoSpot microanalyzer (Cellular Technologies). Data were processed using Prism software (GraphPad Prism 8.0).

Recombinant S-glycoprotein ectodomain and S^B production

The SARS-CoV-2 2P S glycoprotein (GenBank: YP_009724390.1) ectodomain was produced in 500-ml cultures of HEK293F cells grown in suspension using FreeStyle 293 expression medium (Life technologies) at 37 °C in a humidified 8% CO₂ incubator rotating at 130 r.p.m., as previously reported⁶. The culture was transfected using 293fectin (ThermoFisher Scientific) with cells grown to a density of 10⁶ cells per ml and cultivated for 3 d. The supernatant was collected and cells were resuspended for another three days, yielding two collections. Clarified supernatants were purified using a 5-ml Cobalt affinity column (Takara). Purified protein was concentrated and flash-frozen in a buffer containing 20 mM Tris pH 8.0 and 150 mM NaCl before cryo-EM analysis. The SARS-CoV-2 2P S-glycoprotein-avi, SARS-CoV S glycoprotein, HCoV-OC43 S glycoprotein and MERS-CoV S glycoprotein constructs have previously been described^{14,33} and were produced similarly to SARS-CoV-2 2P S glycoprotein.

Cryo-EM sample preparation and data collection

Three microlitres of SARS-CoV-2 S glycoprotein at 1.6 mg/ml was mixed with 0.45 µl of S309 Fab (obtained by LysC fragmentation of S309 IgG) at 7.4 mg/ml for 1 min at room temperature before application onto a freshly glow-discharged 1.2/1.3 UltraFoil grid (300 mesh). Plunge freezing used a vitrobot MarkIV (ThermoFisher Scientific) using a blot force of 0 and 6.5 s blot time at 100% humidity and 25 °C. Data were acquired using the Leginon software⁵⁸ to control an FEI Titan Krios transmission electron microscope operated at 300 kV and equipped with a Gatan K2 Summit direct detector and Gatan Quantum GIF energy filter, operated

in zero-loss mode with a slit width of 20 eV. Automated data collection was carried out using Leginon at a nominal magnification of 130,000× with a pixel size of 0.525 Å with tilt angles ranging between 20° and 50°, as previously described⁵⁹. The dose rate was adjusted to 8 counts per pixel per s, and each movie was acquired in super-resolution mode fractionated in 50 frames of 200 ms. Three thousand nine hundred micrographs were collected in a single session with a defocus range of between -1.0 and -3.0 µm.

Cryo-EM data processing

Movie frame alignment, estimation of the microscope contrast-transfer function parameters, particle picking and extraction were carried out using Warp⁶⁰. Particle images were extracted with a box size of 800 binned to 400, yielding a pixel size of 1.05 Å. For each dataset, two rounds of reference-free 2D classification were performed using cryoSPARC⁶¹ to select well-defined particle images. Subsequently, two rounds of 3D classification with 50 iterations each (angular sampling 7.5° for 25 iterations and 1.8° with local search for 25 iterations), using a previously reported closed SARS-CoV-2 S glycoprotein structure⁶ as initial model, were carried out using Relion⁶² without imposing symmetry to separate distinct SARS-CoV-2 S glycoprotein conformations. Three-dimensional refinements were carried out using non-uniform refinement along with per-particle defocus refinement in cryoSPARC⁶¹. Particle images were subjected to Bayesian polishing⁶³ before performing another round of non-uniform refinement in cryoSPARC⁶¹, followed by per-particle defocus refinement and again non-uniform refinement. Reported resolutions are based on the gold-standard Fourier shell correlation of 0.143 criterion and Fourier shell correlation curves were corrected for the effects of soft masking by high-resolution noise substitution⁶⁴.

Cryo-EM model building and analysis

UCSF Chimera⁶⁵ and Coot were used to fit atomic models (Protein Data Bank codes (PDB) 6VXX and PDB 6VYB) into the cryo-EM maps. The Fab was subsequently manually built using Coot^{66,67}. N-linked glycans were hand-built into the density where visible, and the models were refined and relaxed using Rosetta⁶⁸. Glycan refinement relied on a dedicated Rosetta protocol, which uses physically realistic geometries based on prior knowledge of saccharide chemical properties⁶⁹, and was aided by using both sharpened and unsharpened maps. Models were analysed using MolProbity⁷⁰, EMRinger⁷¹, Phenix⁷² and privateer⁷³ to validate the stereochemistry of both the protein and glycan components. Figures were generated using UCSF ChimeraX⁷⁴.

Crystallization and X-ray structure determination of Fab S309

Fab S309 crystals were grown in a hanging drop set up with a mosquito at 20 °C using 150 nl protein solution in Tris HCl pH 8.0, 150 mM NaCl and 150 nl mother liquor solution containing 1.1 M sodium malonate, 0.1 M HEPES, pH 7.0 and 0.5% (w/v) Jeffamine ED-2001. Crystals were cryo-protected using the mother liquor solution supplemented with 30% glycerol. The dataset was collected at ALS beamline 5.0.2 and processed to 3.3 Å resolution in space group P4₁2₁2 using mosflm⁷⁵ and Aimless⁷⁶. The structure of Fab S309 was solved by molecular replacement using Phaser⁷⁷ and homology models as search models. The coordinates were improved and completed using Coot⁶⁶ and refined with REFMAC5⁷⁸. Crystallographic data collection and refinement statistics are shown in Extended Data Fig. 5g.

Conservation analysis

SARS-CoV-2 genomics sequences were downloaded from GISAID on 27 April 2020 (*n*=11,839) using the 'complete (>29,000 bp)' and 'low coverage exclusion' filters. Bat and pangolin sequences were removed to yield human sequences only. The S glycoprotein ORF was localized by aligning the reference protein sequence (YP_009724390.1) to the genomic sequence of isolates with Exonerate v.2.4.0 (-m protein2dna --refine

Article

full --minintron 999999 --percent 30 --showalignment false --showvulgar false --ryo ">%ti\n%tcs"). Coding nucleotide sequences were translated in silico using seqkit v.0.12.0. Multiple sequence alignment was performed using MAFFT v.7.455 (--amino -bl 80 --nomemsave --reorder --add spike_aa_sequences.fasta --keeplength reference_aa_sequence.fasta). Variants were determined by comparison of aligned sequences to the reference sequence using the R v3.6.3/Bioconductor v.3.10 package Biostrings v.2.54.0 (function: consensusMatrix). A similar strategy was used to extract and translate S glycoprotein sequences from SARS-CoV genomes sourced from ViPR (search criteria: SARS-related coronavirus, full-length genomes, human host, deposited before December 2019 to exclude SARS-CoV-2, $n=53$, performed on 29 March 2020). We confirmed that sourced SARS-CoV genome sequences comprised all the major published strains (such as Urbani, Tor2, TW1, P2, and Frankfurt1, among others). Pangolin sequences⁷⁹ were sourced from GISAID and bat sequences from the three clades of sarbecoviruses³⁹ were downloaded from Genbank (civet (AY304486.1) and raccoon dog (AY304487.1). Full conservation analysis code is available at <https://github.com/virbio/manuscript-cov2-pinto-conservation>.

Reporting summary

Further information on research design is available in the Nature Research Reporting Summary linked to this paper.

Data availability

The cryo-EM maps and atomic models have been deposited at the Electron Microscopy Data Bank and the PDB with accession codes EMD-21864 and 6WPS (closed SARS-CoV-2 S in complex with S309), as well as EMD-21865 and 6WP (SARS-CoV-2 S with one S^B open in complex with S309). The crystal structure of the S309 Fab was deposited to the PDB with accession code 6WS6. Materials generated in this study will be made available on request, but we may require a completed materials transfer agreement.

55. Stettler, K. et al. Specificity, cross-reactivity, and function of antibodies elicited by Zika virus infection. *Science* **353**, 823–826 (2016).
56. Zalevsky, J. et al. Enhanced antibody half-life improves in vivo activity. *Nat. Biotechnol.* **28**, 157–159 (2010).
57. Tian, X. et al. Potent binding of 2019 novel coronavirus spike protein by a SARS coronavirus-specific human monoclonal antibody. *Emerg. Microbes Infect.* **9**, 382–385 (2020).
58. Suloway, C. et al. Automated molecular microscopy: the new Leginon system. *J. Struct. Biol.* **151**, 41–60 (2005).
59. Tan, Y.Z. et al. Addressing preferred specimen orientation in single-particle cryo-EM through tilting. *Nat. Methods* **14**, 793–796 (2017).
60. Tegunov, D. & Cramer, P. Real-time cryo-electron microscopy data preprocessing with Warp. *Nat. Methods* **16**, 1146–1152 (2019).
61. Punjani, A., Rubinstein, J. L., Fleet, D. J. & Brubaker, M. A. cryoSPARC: algorithms for rapid unsupervised cryo-EM structure determination. *Nat. Methods* **14**, 290–296 (2017).
62. Zivanov, J. et al. New tools for automated high-resolution cryo-EM structure determination in RELION-3. *eLife* **7**, e42166 (2018).
63. Zivanov, J., Nakane, T. & Scheres, S. H. W. A Bayesian approach to beam-induced motion correction in cryo-EM single-particle analysis. *IUCrJ* **6**, 5–17 (2019).
64. Scheres, S. H. & Chen, S. Prevention of overfitting in cryo-EM structure determination. *Nat. Methods* **9**, 853–854 (2012).
65. Goddard, T. D., Huang, C. C. & Ferrin, T. E. Visualizing density maps with UCSF Chimera. *J. Struct. Biol.* **157**, 281–287 (2007).

66. Emsley, P., Lohkamp, B., Scott, W. G. & Cowtan, K. Features and development of Coot. *Acta Crystallogr. D* **66**, 486–501 (2010).
67. Brown, A. et al. Tools for macromolecular model building and refinement into electron cryo-microscopy reconstructions. *Acta Crystallogr. D* **71**, 136–153 (2015).
68. Wang, R. Y. et al. Automated structure refinement of macromolecular assemblies from cryo-EM maps using Rosetta. *eLife* **5**, e17219 (2016).
69. Frenz, B. et al. Automatically fixing errors in glycoprotein structures with Rosetta. *Structure* **27**, 134–139.e3 (2019).
70. Chen, V. B. et al. MolProbity: all-atom structure validation for macromolecular crystallography. *Acta Crystallogr. D* **66**, 12–21 (2010).
71. Barad, B. A. et al. EMRinger: side chain-directed model and map validation for 3D cryo-electron microscopy. *Nat. Methods* **12**, 943–946 (2015).
72. Liebschner, D. et al. Macromolecular structure determination using X-rays, neutrons and electrons: recent developments in Phenix. *Acta Crystallogr. D* **75**, 861–877 (2019).
73. Aguirre, J. et al. Privateer: software for the conformational validation of carbohydrate structures. *Nat. Struct. Mol. Biol.* **22**, 833–834 (2015).
74. Goddard, T. D. et al. UCSF ChimeraX: Meeting modern challenges in visualization and analysis. *Protein Sci.* **27**, 14–25 (2018).
75. Battye, T. G., Kontogiannis, L., Johnson, O., Powell, H. R. & Leslie, A. G. iMOSFLM: a new graphical interface for diffraction-image processing with MOSFLM. *Acta Crystallogr. D* **67**, 271–281 (2011).
76. Evans, P. R. & Murshudov, G. N. How good are my data and what is the resolution? *Acta Crystallogr. D* **69**, 1204–1214 (2013).
77. McCoy, A. J. et al. Phaser crystallographic software. *J. Appl. Crystallogr.* **40**, 658–674 (2007).
78. Murshudov, G. N. et al. REFMAC5 for the refinement of macromolecular crystal structures. *Acta Crystallogr. D* **67**, 355–367 (2011).
79. Lam, T. T. et al. Identifying SARS-CoV-2-related coronaviruses in Malayan pangolins. *Nature* <https://doi.org/10.1038/s41586-020-2169-0> (2020).

Acknowledgements This study was supported by the National Institute of General Medical Sciences (R01GM120553, D.V.), the National Institute of Allergy and Infectious Diseases (HHSN272201700059C to D.V. and 75N93019C00062 to M.S.D.), a Pew Biomedical Scholars Award (D.V.), an Investigators in the Pathogenesis of Infectious Disease Award from the Burroughs Wellcome Fund (D.V.), the University of Washington Arnold and Mabel Beckman cryo-EM centre, the Pasteur Institute (M.A.T.) and beamline 5.0.2 at the Advanced Light Source at Lawrence Berkley National Laboratory. Beamline 5.0.2 is supported by The Berkeley Center for Structural Biology. The Advanced Light Source is a Department of Energy Office of Science User Facility under Contract No. DE-AC02-05CH1231. We thank N. Zheng for use of his crystallization robot. We gratefully acknowledge the authors, originating and submitting laboratories of the sequences from GISAID's EpiFlu Database upon which this research is based.

Author contributions A.C.W., K.F., M.S.D., D.V. and D.C. designed the experiments. A.C.W., M.A.T., S.J. and E.C. expressed and purified the proteins. K.C., F.Z., S.J. and E.C. sequenced and expressed antibodies. D.P., M.B., A.C.W. and S.B. performed binding assays. D.P., M.B., A.C.W., A.P. and A.D.M. carried out pseudovirus neutralization assays. J.B.C. and R.E.C. performed neutralization assays with authentic SARS-CoV-2. B.G. performed effector function assays. Y.-J.P. prepared samples for cryo-EM and collected the data. Y.-J.P. and D.V. processed the data, built and refined the atomic models. A.C.W. crystallized the S309 Fab. Y.-J.P. collected and processed the X-ray diffraction data and built and refined the atomic model. R.S., A.T. and G.S. performed bioinformatic and conservation analysis. A.L. provided key reagents. A.C.W., K.F., C.H.-D., H.W.V., A.L., D.V. and D.C. analysed the data and prepared the manuscript with input from all authors.

Competing interests D.P., S.B., K.C., E.C., C.H.-D., G.S., M.B., A.K., K.F., A.P., F.Z., S.J., B.G., A.D.M., A.L., A.T., H.W.V., R.S. and D.C. are employees of Vir Biotechnology and may hold shares in Vir Biotechnology. M.S.D. is a consultant for Inbios, Eli Lilly, Vir Biotechnology, NGM Biopharmaceuticals and Emergent BioSolutions, and on the Scientific Advisory Board of Moderna. The Diamond laboratory at Washington University School of Medicine has received sponsored research agreements from Moderna. The other authors declare no competing interests.

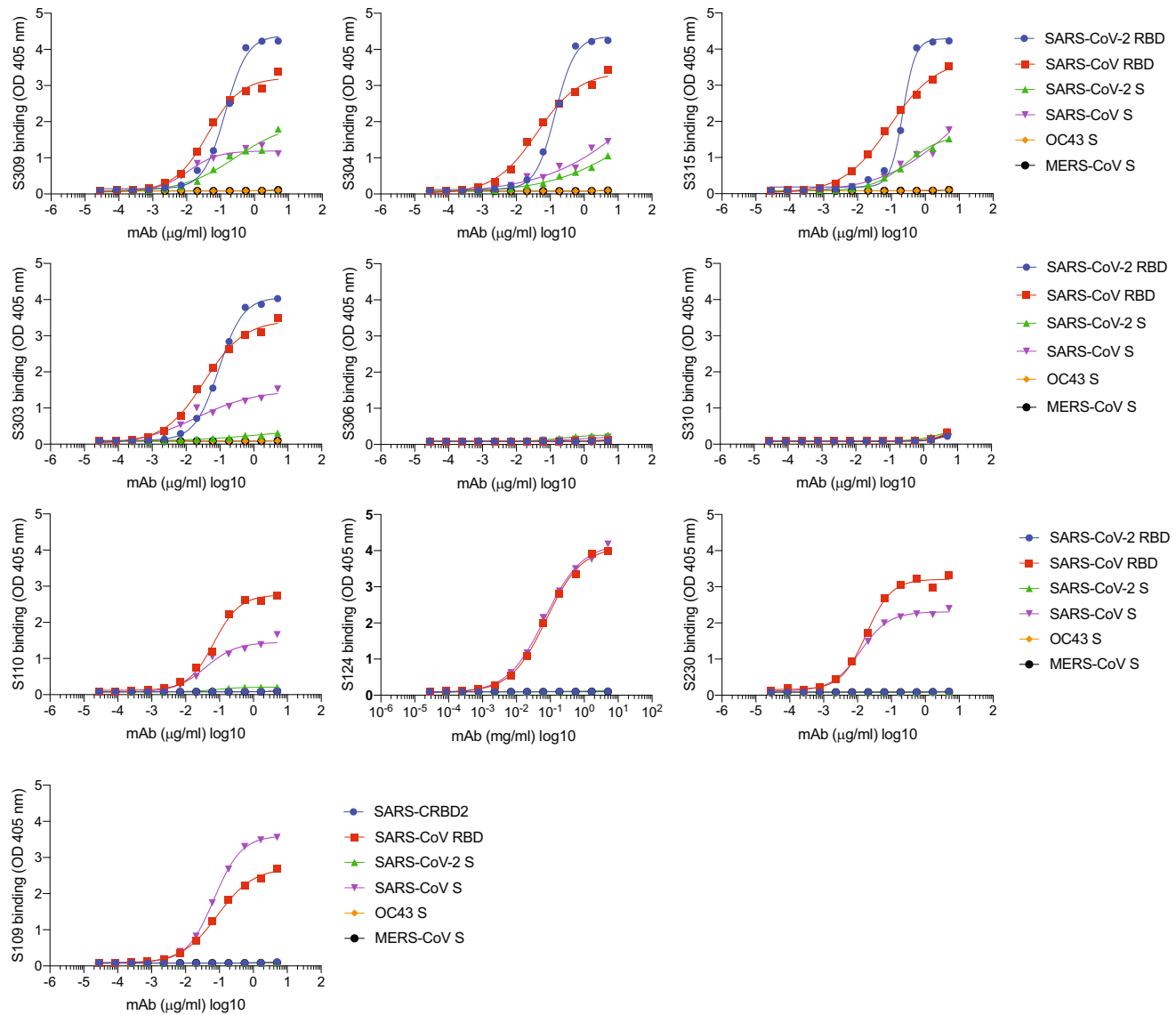
Additional information

Supplementary information is available for this paper at <https://doi.org/10.1038/s41586-020-2349-y>.

Correspondence and requests for materials should be addressed to D.V. or D.C.

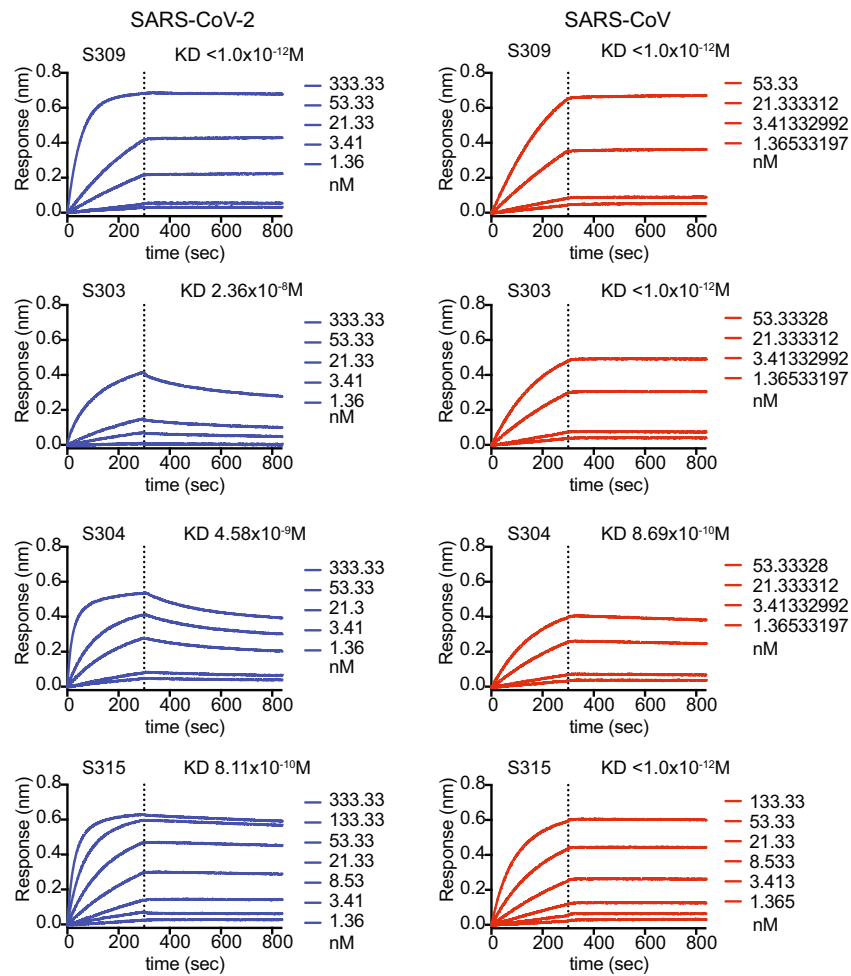
Peer review information *Nature* thanks Pamela Bjorkman, Michel Nussenzweig and the other, anonymous, reviewer(s) for their contribution to the peer review of this work.

Reprints and permissions information is available at <http://www.nature.com/reprints>.



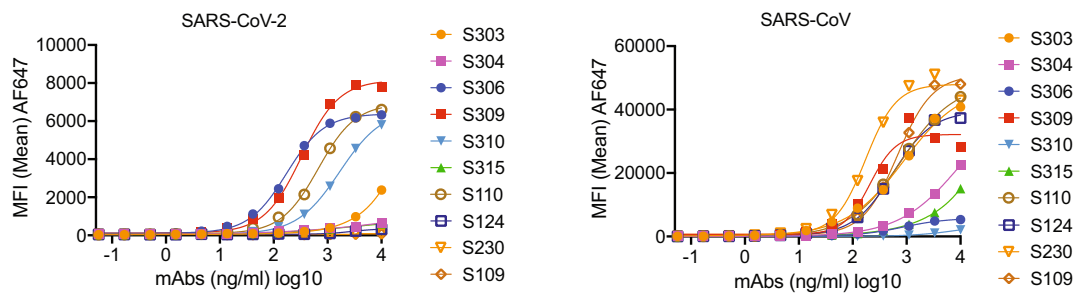
Extended Data Fig. 1 | Binding of cross-reactive antibodies to RBD of SARS-CoV and SARS-CoV-2, and to ectodomains of different coronavirus strains. mAbs were tested by enzyme-linked immunosorbent assay at a concentration range of 5 to $0.00028 \mu\text{g ml}^{-1}$. S, stabilized prefusion trimer of

the indicated coronavirus. Symbols show mean of duplicates. The full dataset was tested once. Binding of S309 to the RBDs and all S glycoproteins was repeated in an independent experiment with similar results.

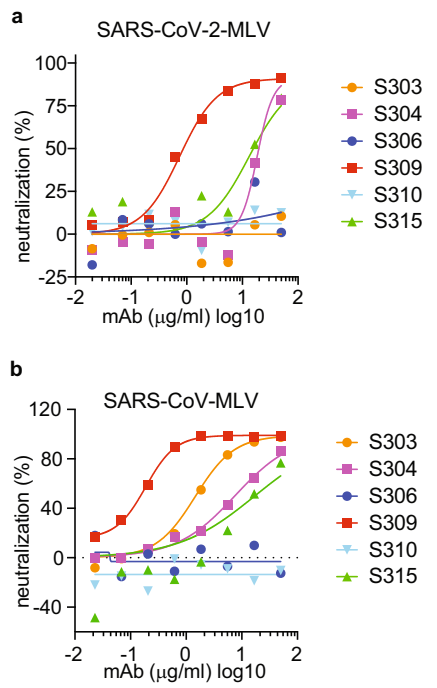


Extended Data Fig. 2 | Antibody affinity and avidity of S309, S303, S304 and S315 to the RBD of SARS-CoV and SARS-CoV-2. Antibodies were loaded to biolayer interferometry (BLI) pins via protein A for the measurement of association of different concentrations of the RBD of SARS-CoV-2 (blue) and

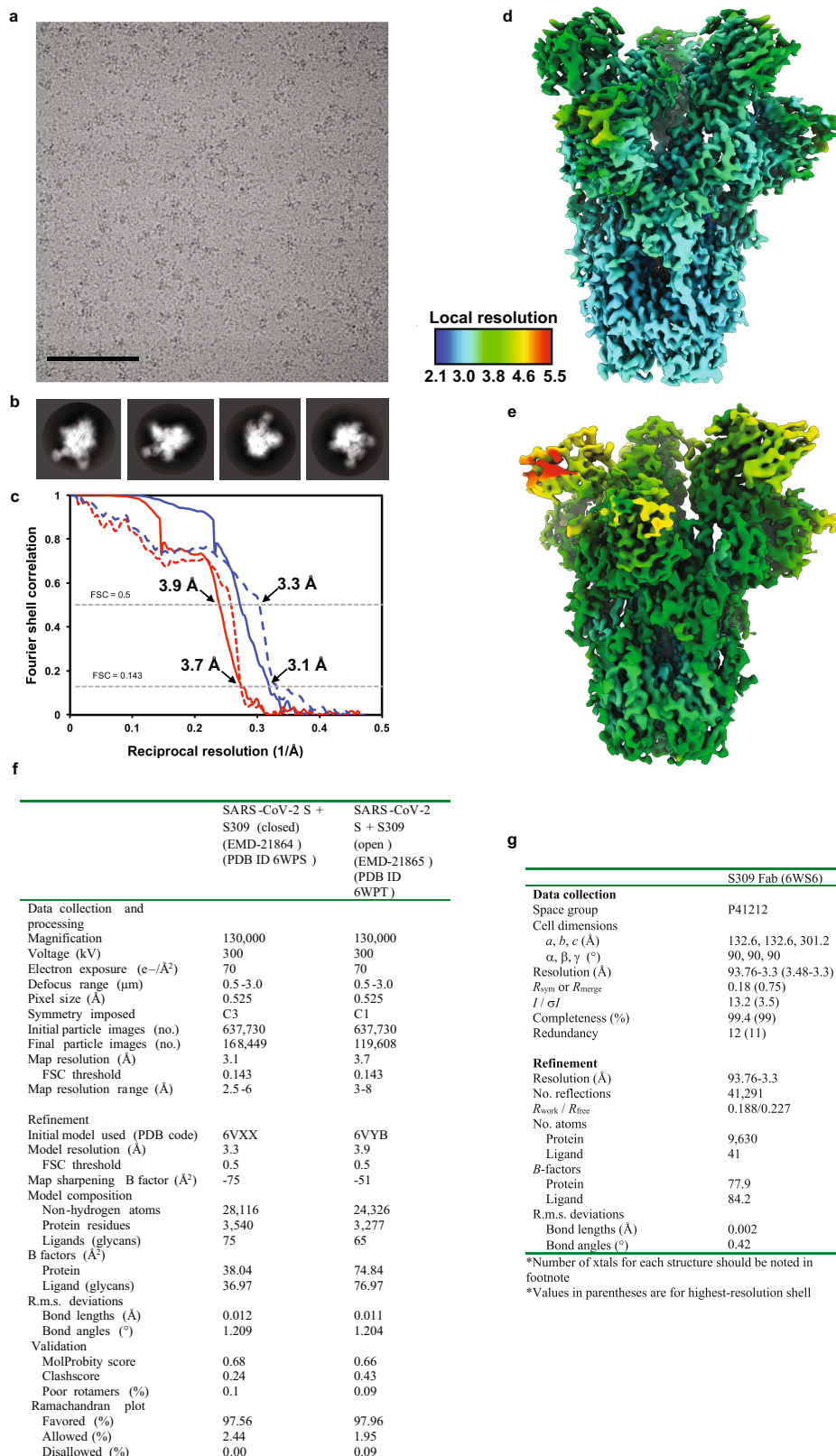
SARS-CoV (red). Vertical dashed lines indicate the start of the dissociation phase, when BLI pins were switched to buffer. The experiments were done once for S303, S304 and S315. The experiment for S309 was repeated once.



Extended Data Fig. 3 | Binding of crossreactive mAbs to expiCHO cells transfected with SARS-CoV or SARS-CoV-2 S glycoprotein. Mean fluorescence intensity as measured in flow cytometry for each antibody. Antibody concentrations tested are indicated in the x axis.



Extended Data Fig. 4 | Neutralization of cross-reactive mAbs. **a, b**, The six cross-reactive mAbs indicated in the legend were tested for neutralization of SARS-CoV-2-MLV (**a**) and SARS-CoV-MLV (**b**). Symbols are mean of duplicates. **a**, One experiment. Neutralization of S304, S315 and S309 was tested in at least two independent experiments with similar results. **b**, One out of two experiments with similar results.



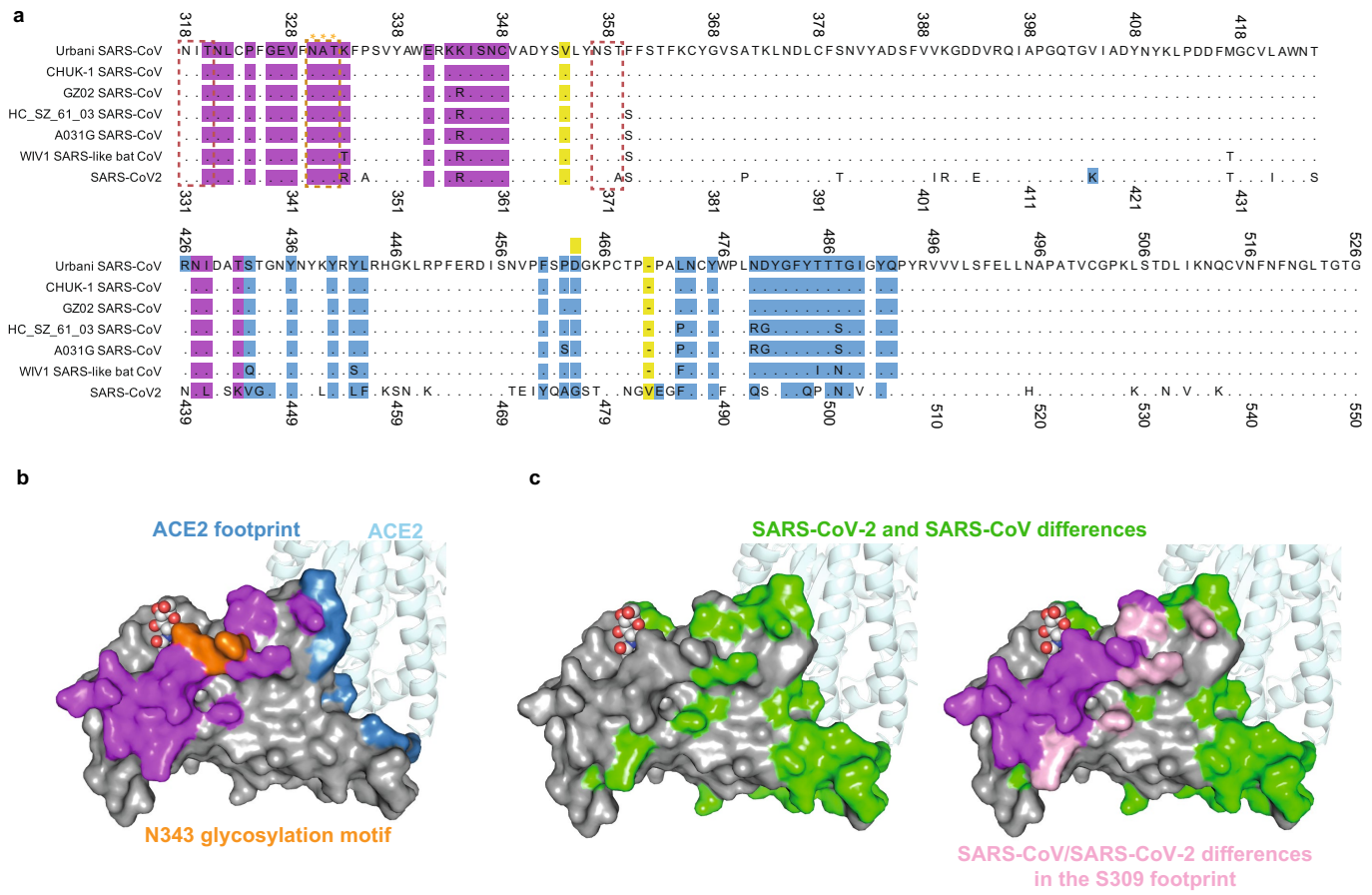
Extended Data Fig. 5 | Cryo-EM data processing and validation.

a, b, Representative electron micrograph (**a**) and class averages (**b**) of SARS-CoV-2 S glycoprotein embedded in vitreous ice. Scale bar, 100 nm. **c,** Gold-standard (solid line) and map/model (dashed line) Fourier shell correlation curves for the closed (blue) and partially open trimers (red).

The 0.143 and 0.5 cutoffs are indicated by horizontal grey dashed lines.

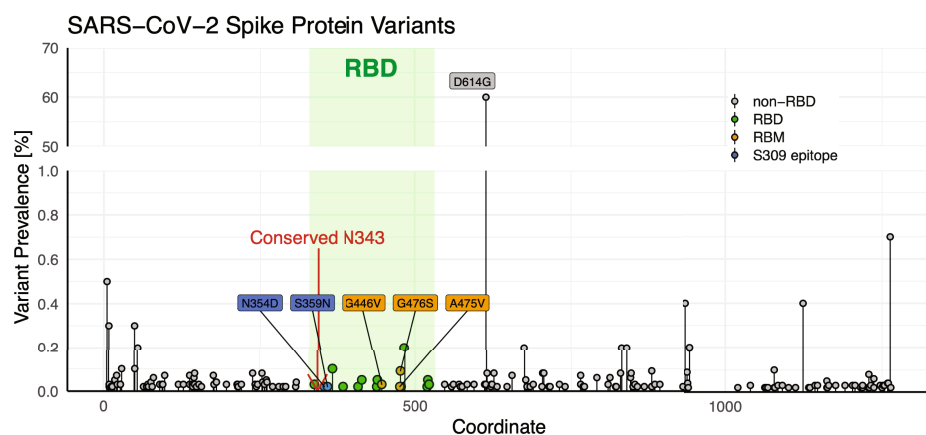
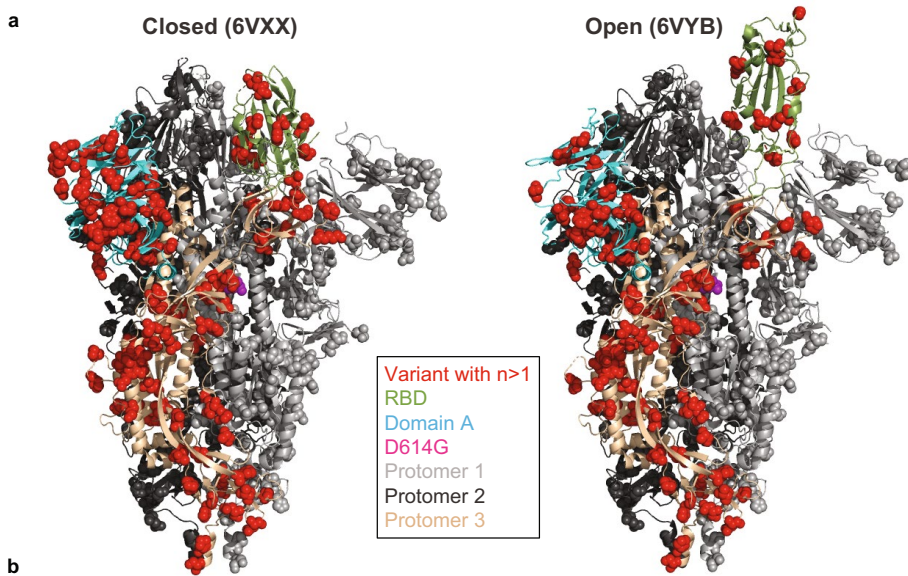
d, e, Local-resolution maps calculated using cryoSPARC for the closed- (**d**) and open- (**e**) state reconstructions. **f,** Cryo-EM data collection, refinement and validation statistics. **g,** Data collection and refinement statistics for the S309 Fab X-ray structure.

Article



Extended Data Fig. 6 | Conservation of spike and RBD residues. **a**, Alignment of the full RBD of multiple sarbecoviruses. The ACE2 and S309 footprints are highlighted in blue and magenta, respectively. Dashed boxes indicate glycosylation sites and orange asterisks indicate the N343 glycosylation site. **b**, ACE2 and S309 footprints mapped onto the structure of the SARS-CoV-2 RBD domain (PDB 6M0J). The ACE2 footprint was defined by residues being

within 5 Å of the receptor in 6M0J. The highly conserved NAT glycosylation motif is shown in orange. **c**, The SARS-CoV and SARS-CoV-2 differences are shown in green, and differences within the S309 footprint are shown in pink (right). The high-frequency RBD variants are shown in yellow (second from left; 4 out of 8 are visible). Red spheres indicate the position of the N343 glycan.



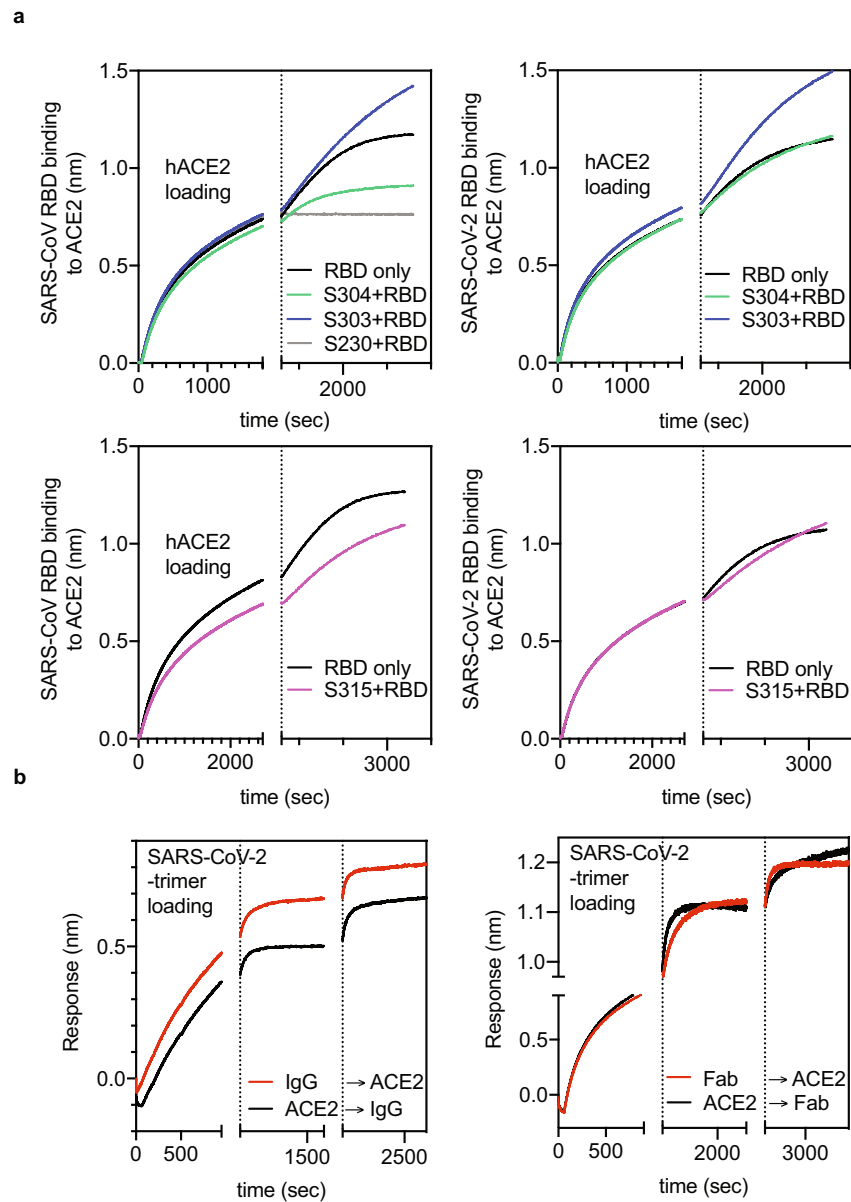
c

	SARS-CoV-2 pos.	333	334	335	337	339	340	341	343	344	345	346	354	356	357	358	359	360	361	440	441	444	509	n	IC50 (μg/ml)
	SARS-CoV pos.	320	321	322	324	326	327	328	330	331	332	333	341	343	344	345	346	347	348	427	428	431	495		
Sarbecoviruses	Human SARS-CoV-2	T	N	L	P	G	E	V	N	A	T	R	N (D)	K	R	I	S (N)	N	C	N	L	K	R	11839	0.24
	GD Pangolin	-	-	-	-	-	-	-	-	-	-	T	-	-	-	-	-	-	-	-	-	-	2		
	Bat CoV RaTG13	-	-	-	-	-	-	-	-	-	-	T	-	-	-	-	-	-	-	H	I	-	-	6	
	GX Pangolin	-	-	-	-	-	-	-	-	-	-	S	K	-	-	-	-	-	-	K	Q	L	-		
	Bat CoVs ZC45, ZXC21	-	-	V	-	H	K	-	-	-	-	-	E	T	K	-	-	D	-	K	Q	-	-	2	
Clade 3	Human SARS-CoV	-	-	-	-	-	-	-	-	-	-	K	E	-	K/R	-	-	-	-	I	T	-	-	53	0.12-0.15
	Civet SARS-CoV SZ3	-	-	-	-	-	-	-	-	-	-	K	E	-	-	-	-	-	-	I	T	-	-		
	Raccoon Dog SARS-CoV SZ13	-	-	-	-	-	-	-	-	-	-	K	E	-	-	-	-	-	-	I	T	-	-		
	Bat CoV WIV16	-	-	-	-	-	-	-	-	-	-	-	E	-	-	-	-	-	-	I	T	-	-		
	Bat CoV WIV1	-	-	-	-	-	-	-	-	-	-	T	E	-	-	-	-	-	-	I	T	-	-	21	0.18
Clade 1	Other Bat CoVs	-	-	R/-	-	D/-	K/-R	-I	-	-V	-S	-T	E	T/-I	K/-	-	-	D/-E	-	K/-Q	Q/-H	G/T/S	-		
	Bat CoV BtKY72	-	-	-	-	-	-	Q	-	-	-	S	N	E	L	-	-	-	D	-	S	V	-	-	
	Bat CoV BGR2008	-	Q	-	-	N	-	-	I	-	S	E	M	-	-	T	-	-	S	-	-	-			

Extended Data Fig. 7 | Conservation of Sglycoprotein and RBD residues.

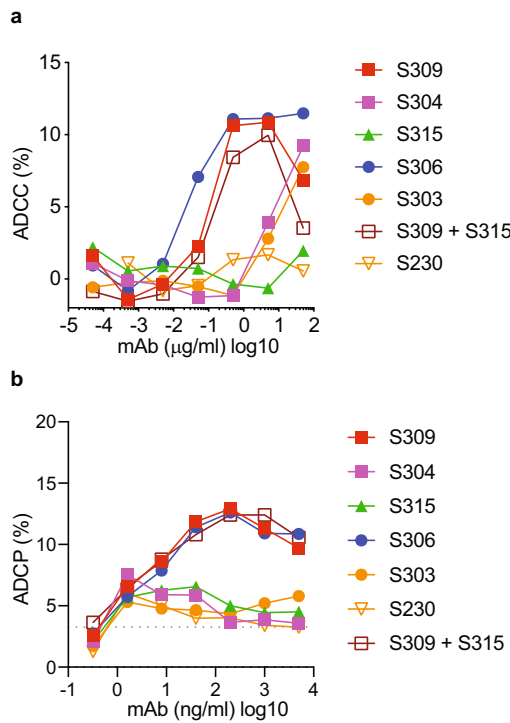
SARS-CoV-2 genome sequences retrieved from GISAID on 27 April 2020 ($n=11,839$) were used to annotate variants of the S glycoprotein. Only variants supported by at least 2 sequences (prevalence greater than 0.01%) are shown. **a**, Residues with variants are rendered as red spheres mapped onto the closed and open form of the full trimeric ectodomain ($n=171$). **b**, Variants are plotted by amino acid position. Each dot is a distinct variant. Colour encodes location (RBD, RBM or S309 epitope). Variants are labelled if their prevalence is greater than 1% (only D614G) or if they belong to the RBM or the S309 epitope. The location of conserved N343 is indicated. **c**, Conservation of residues making contact with S309 across clades of Sarbecovirus. Summary of residue variation observed in human and animal SARS-related coronaviruses, arranged by

clades³⁹. Residue coordinates for both SARS-CoV-2 and SARS-CoV are shown. The NAT motif that directs glycosylation of N343 is highlighted in orange. Substitutions between SARS-CoV and SARS-CoV-2 residues are marked in pink. Dashes indicate identity to SARS-CoV-2 consensus residues. Blanks indicate deletions. When multiple variants are found, they are listed in order of prevalence (from high to low). When $n > 10,000$ (SARS-CoV-2), variants found in a single sequence are not shown, and variants found in 2 sequences only are parenthesized. For the 21 sequences of clade-3 bat CoV-2 from ref. ³⁹ at most the top-3 variants at each position are shown. n , number of analysed sequences. IC₅₀, half maximal neutralizing concentration of S309 against SARS-CoV-2-MLV or SARS-CoV.



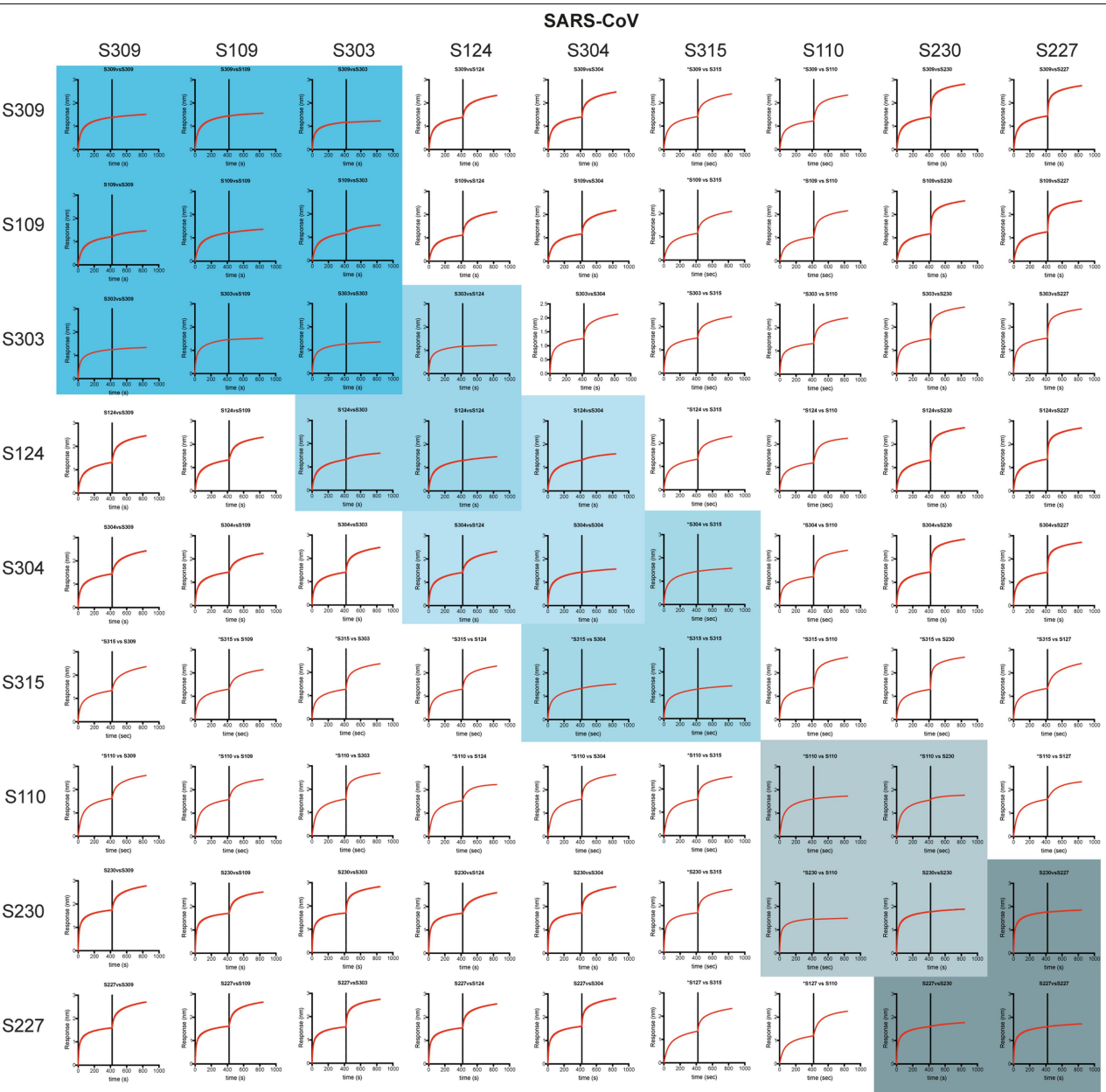
Extended Data Fig. 8 | Competition of antibodies with RBD binding to ACE2. **a**, Human ACE2 (hACE2) was loaded onto BLI sensors, followed by incubation of the sensors with RBD alone or RBD in combination with recombinant antibodies. The vertical dashed line indicates the start of the loading of RBD with or without antibody. **b**, SARS-CoV-2 ectodomain was

loaded onto BLI sensors, followed by incubation of the sensors with macaque ACE2 or S309 IgG (left) or Fab (right). In a third step, sensors were incubated with macaque ACE2 or S309 IgG or Fab as indicated. The experiments were conducted once.



Extended Data Fig. 9 | ADCC and ADCP data for one representative donor.

This figure is related to Fig. 3. **a**, ADCC for one donor who is homozygous for high-affinity variant Fc γ RIIIa 158V (VV). Background signal of cells without antibody was deducted from all values before plotting. **b**, ADCP for one donor who is heterozygous for Fc γ RIIIa 158V (FV). The dashed line indicates the background signal for cells without antibody. Symbols are mean of duplicates. Cells from each donor were sufficient to conduct one experiment.



Extended Data Fig. 10 | Competition of mAb pairs for binding to the RBD domain of SARS-CoV, as determined by BLI (Octet). RBD was loaded on BLI pins. Association was measured first for antibodies indicated on the left of the

matrix, followed by association of the antibodies indicated on top of the matrix. Each combination of antibodies was tested once.

